Experimental apparatus for universal spin-motion control in multi-ion registers

Donovan Webb

St Peter's College

University of Oxford

A thesis submitted for the degree of

Confirmation of Status

Trinity 2025

Contents

0.1   Motivation

The following chapter details the characterisation work performed during the commisioning of a new ion trap apparatus. Over the past two years, my colleagues and I have been constructing this system, which is now approaching readiness for our desired experiments. In this *Motivation* section, I will provide a high-level overview of the physics we want to explore, state the unique aspects of the apparatus that enable these experiments, and finally, give a timeline for planned future work. The complexity of our system neccesitates collaboration, and so I would like to acknowledge the rest of the *FastGates* team, for their extensive contributions to bringing the system online.

There are two research directions that we are pursuing with this apparatus. Both involve the interplay between the "spin" electronic degrees of freedom and the motion of the ions which we describe by quantum harmonic oscillators.
The first is the demonstration of fast, high-fidelity two-qubit entangling gates between trapped ions. High-fidelity entangling gates are critical for developing a quantum computer which can perform useful calculations with high success probability [1]. Gate errors associated with decoherence of the quantum state are often dominated by incoherent processes, such as spontaneous emission, or interactions between the qubit and the environment [2]. These errors accumulate with time, and so may be mitigated by increasing the algorithm "clock-speed", hence our desire for fast entanglement [3, 4]. Typically in ion traps, local two-qubit gates are performed via the ion's shared motion, which may be excited by interaction with a laser [5, 6]. As the effective Rabi frequency approaches that of the frequency separation of the motional modes, the dynamics between spin and motion become complicated by multiple simultaneous mode excitations [4]. Our apparatus is designed to provide the required laser intensities and mode frequencies such that we can explore this regime, and demonstrate the required control to tame these multiple mode excitations and perform high-fidelity entangling gates.
The second direction is the use of the motion of the ion directly as a quantum

resource [7, 8]. This falls into the continuous variable quantum computing paradigm (CVQC), where instead of discrete qubits, the quantum state is described by bosonic "qumodes" [9]. CVQC reduces the technical overhead of scaling discrete systems, as larger Hilbert spaces are easily accessed due to the many level nature of the individual qumodes. We want to demonstrate a universal set of gates for CVQC, which includes, single-mode Gaussian and non-Gaussian gates (demonstrated in [10]), and two-mode entangling gates. Further, we want to demonstrate the ability to simultaneously leverage both bosonic and spin degrees of freedom of our ions to efficiently encode problems in the full hybrid system we have access to [11, 12]. Our apparatus has both precise motional control and stability through our trap choice, and the individual addressing system that is required when interacting with many-ion chains.

Details of the apparatus are presented in the Appendices. Summarised here are the unique aspects enabling the desired experiments:

- **High laser intensities:** The system is designed to provide high laser intensities, which are required to drive fast entangling gates. This is achieved through the use of a 5 W Ti:Sapph system (section A.5.1) and two high numerical aperture (NA = 0.6) objectives (section A.3).

- **Single ion addressing:** Using crossed acousto-optic deflectors, we can selectively address individual ions in a multi-ion chain (section A.5.2). This enables fast entangling gates between ions in a long chain, and the ability to perform motional interactions on selected modes.

- **Standing wave addressing:** The system is designed to provide standing optical waves at the ion position. Standing waves are required for some fast gate schemes [13].

- **Motional control:** The Paul trap used in the system, produced by *National Physical Laboratory* in the UK, has low heating rates (section 1.3.2), deep trapping potentials relative to surface style ion traps, and flexible control over

DC confinement (section A.1) (e.g. ion shuttling). Low heating rates are required for long motional coherence times (section 1.3.3).

Here, the characterisation of the spin qubits is in the context of discrete variable quantum computing. We are interested in the fidelity of qubit state-preparation (section 1.2.1), measurement (section 1.2.2), single- (section 1.2.3) and two-qubit gates (section 1.4.2). These individual elements comprise longer circuits, and so all contribute to the overall fidelity of any chosen algorithm.

The motional characterisation is currently focused on the stability of the modes (section 1.3.3), and the ability to perform spin-dependent forces, SDFs (section 1.4.1). SDFs are the base interaction on which many of the desired CVQC gates are comprised [14], and so these must be well characterised and understood in our system.

To push the system forwards, in the next 6 months, we will focus on commisioning the single addressing system, and on demonstrating squeezing of the motional state of the ion.

As described above, the single addressing system is a critical component for many of our planned experiments. Section A.5.2, and [15] describe the system in detail. The immediate next steps are to align the constructed optical system to the ion chain, and to implement the logical and RF control system required to drive the acousto-optic deflectors. Once this is complete, we will characterise the crosstalk of the system by performing single addressing of ions in a chain and measuring spin populations. We will then be able to demonstrate fast entangling gates between ions in a chain, and the ability to perform motional interactions on selected modes. Squeezing of the motional mode via the method outlined in [14], is a significant step towards demonstrating the universal set of gates for CVQC. The constituent interactions of the effective squeezing gate (two SDFs), are the same interactions needed for trisqueezing [10, 16] — a non-Gaussian gate, and for two-mode squeezing [17] — an entangling gate. Furthermore, once we have demonstrated generating squeezing characteristic functions, there is a clear path to experimentally demonstrating the

extraction of Feynman diagram terms with the hybrid system being used as a quantum simulator [11].

1

Experimental Characterisation

Contents

Before we can proceed with our planned experiments involving the motion and spin of the atoms, the apparatus must be characterised. This characterisation serves two purposes: it allows us to benchmark the performance of our system against state-of-the-art results, and it reveals any current limitations that must be addressed before we can successfully carry out the experiments.

As discussed above, we are interested in two paradigms: discrete variable quantum computing (DVQC), that concerns the manipulation of qubits (or spins), and

continuous variable quantum computing (CVQC), that concerns the manipulation of qumodes (or harmonic motion).

For DVQC, we must have access to the following elementary operations:

- Qubit state preparation, here via optically pumping the electronic state of the ion into one sublevel of the $4S_{1/2}$ manifold — the lower level of our qubit, section 1.2.1.

- Measurement of the qubit state, here via state-dependent fluorescence, section 1.2.2.

- Single qubit rotations, here via interaction with the 729-nm laser, section 1.2.3

- Two qubit entangling-gates, here via spin-dependent forces (SDFs), using the 729-nm laser and the motional modes of the ion, section 1.4.2.

For CVQC, we need:

- Motional state preparation, here via Doppler cooling and sideband cooling, section 1.3.1.

- Measurement of the motional state, which is not yet implemented on our system but will follow [18].

- Single and two qumode gates, which are also not yet implemented, but will utilise SDFs following [14], section 1.4.1.

We split this chapter into interactions involving only the spin, then those focussed only on the motion, and finally we describe spin-motion interactions. First, however, we describe the ion, its level structure, and the relevant lasers to manipulate its state.
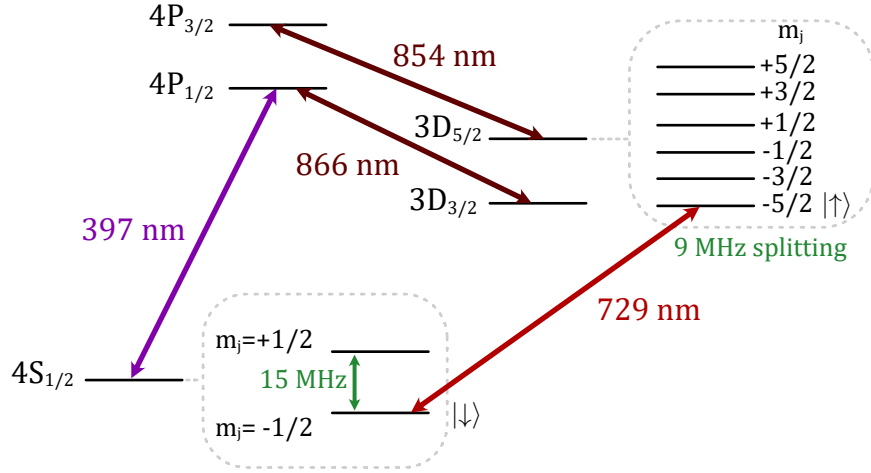
Figure 1.1: Electronic energy levels of $^{40}\text{Ca}^+$, which will be used in this thesis. The levels are split by the Zeeman effect due to a 5.4 G external magnetic field (they are shown explicitly only for the qubit manifolds). The transitions marked are required for cooling and control over the ion. The chosen qubit levels are labelled with $|\downarrow\rangle$, $|\uparrow\rangle$.

1.1 The Ion

The $^{40}\text{Ca}^+$ion has a rich level structure, shown in figure 1.1, with many accessible quadrupole transitions $4S_{1/2} \leftrightarrow 3D_{5/2}$. The quadrupole transition is ideal for use as a qubit due to the long-lived metastable level ($\tau = 1.1$ s) [19], and the ability to optically couple the transition via a laser. As mentioned in section A.5.1, the 729-nm beam is used for this purpose. By selecting the appropriate frequency of the 729-nm beam, qubit operations such as state preparation (section 1.2.1) and single qubit gates (section 1.2.3) may be driven, or by setting the detuning such that a motional sideband is near resonance, to couple the spin and motional degrees of freedom (section 1.4.1). Here, we discuss which quadrupole transitions are used, and the rationale behind their choice.

Zeeman splitting of the $4S_{1/2}$ and $3D_{5/2}$ states leads to 2 and 6 non-degenerate sublevels, respectively. Due to the magnetic field strength of 5.4 G (section A.2), the S-levels are split by $\sim$15 MHz, and the D-levels by $\sim$9 MHz. This splitting is considerably larger than both the natural linewidth of the 729-nm transition ($\sim$Hz), and the Ti:Sapph laser linewidth ($<$1 kHz), meaning the transitions can be selectively addressed by frequency tuning of the laser. There is some freedom
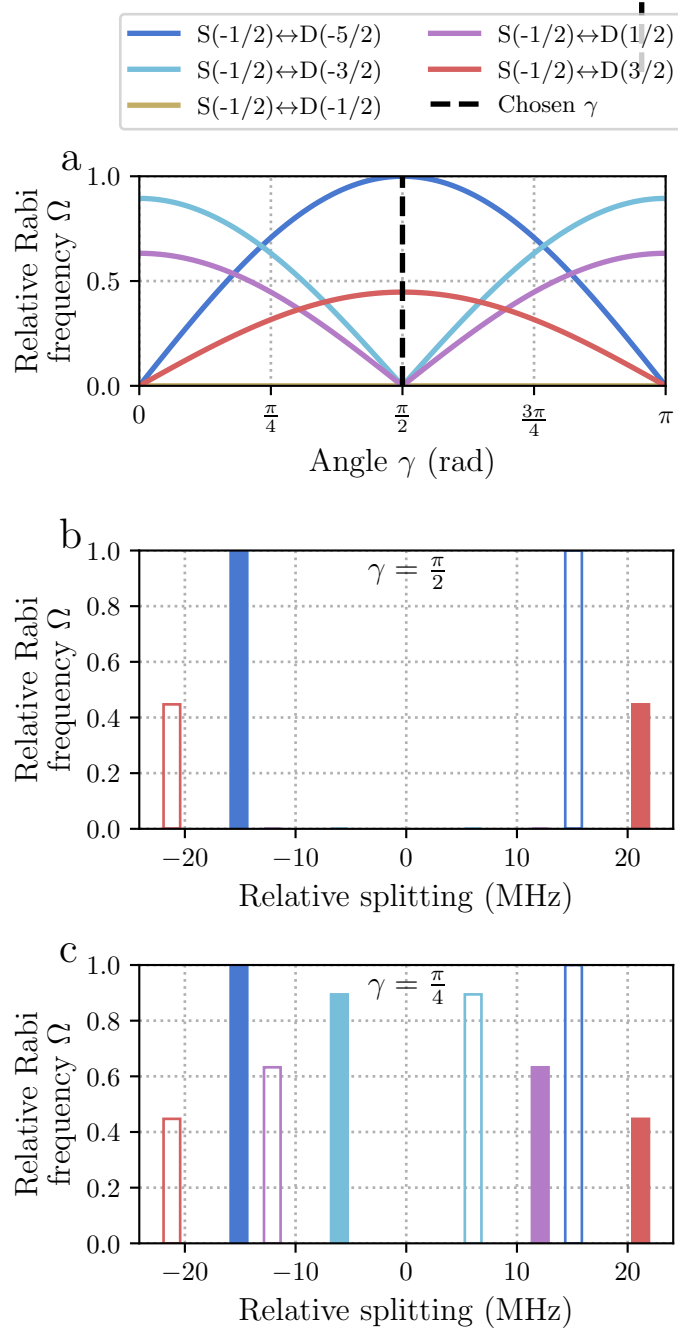
Figure 1.2: Normalised quadrupole Rabi frequencies, Ω, and frequency splittings for the $4S_{1/2} \leftrightarrow 3D_{5/2}$ Zeeman sublevels in ^{40}Ca$^+$. Solid bars correspond to transitions with lower state $|4S_{1/2},\ m_j = -1/2\rangle$, while open bars correspond to transitions with lower state $|4S_{1/2},\ m_j = +1/2\rangle$. **a)** Relative Rabi frequencies as angle γ between the polarisation vector and the magnetic field is varied. The k-vector of the light is assumed to be perpendicular to the B-field. **b)** Relative frequency splittings and strengths when $\gamma = \pi/2$. This is the polarisation chosen for the current and future experiments to reduce the number of transitions which can cause off-resonant interactions when the qubit defined by $|4S_{1/2},\ m_j = -1/2\rangle \leftrightarrow |3D_{5/2},\ m_j = -5/2\rangle$ is used. **c)** Relative frequency splittings and strengths when $\gamma = \pi/4$. At this angle, all transitions are accessible apart from those with $\Delta m_j = 0$. This is the polarisation chosen for our initial experiments to allow access to all transitions for characterisation.

in choosing which of these 10 possible (with $\Delta m_j \leq 2$) quadrupole transitions we define as our qubit. Each transition has a varying coupling strength, here denoted by the relative Rabi frequency, Ω, depending on the polarisation and k-vector of the interacting light with respect to the B-field axis. The desired criteria for qubit and polarisation choice are as follows:

- Access to a closed-cycle transition for sideband cooling, (for details on this, see section 1.3.1). Closed-cycle here means $|4S_{1/2}, \; m_j = -1/2\rangle \rightarrow |3D_{5/2}\rangle \rightarrow |4P_{3/2}, \; m_j = -3/2\rangle \rightarrow |4S_{1/2}, \; m_j = -1/2\rangle$.

- The qubit transition needs a large quadrupole matrix element, leading to a high Rabi frequency, Ω, to enable laser-power-efficient, fast, gates. Polarisation, γ, may be optimised to increase this coupling.

- Ideally the qubit transition should have a low magnetic field sensitivity, to reduce the effect of magnetic field noise. Using a MuMetal enclosure around the experiment does relax this constraint, see section A.2.

- To reduce the effects of off-resonant interactions due to nearby transitions, it is desirable to limit the number of accessible transitions near to the qubit transition. This is done by selecting a polarisation, γ, such that unwanted transitions are suppressed.

Given these criteria, we use the transition $|4S_{1/2}, \; m_j = -1/2\rangle \leftrightarrow |3D_{5/2}, \; m_j = -5/2\rangle$ with magnetic field sensitivity $-0.446 \, \text{MHz} \, \text{G}^{-1}$. Closed-cycle sideband cooling is possible with this same transtion, and state preparation via optical pumping is done via $|4S_{1/2}, \; m_j = +1/2\rangle \leftrightarrow |3D_{5/2}, \; m_j = -3/2\rangle$ with magnetic field sensitivity $-0.624 \, \text{MHz} \, \text{G}^{-1}$.

Figure 1.2 a, shows the normalised Rabi frequencies of each transition as the angle γ between polarisation vector and B-field is varied. Here only linearly-polarised light with k-vector perpendicular to the B-field direction is considered. The polarisation of the 729-nm laser is set to $\gamma = \pi/2$ (black dashed line), which maximises the Rabi frequency of the qubit transition, while suppressing nearby

Parameter	Value
729-nm laser power	1000 µW
729-nm laser detuning	0 MHz*
729-nm pulse duration	5 µs
854-nm laser power	60 µW, $250 \times I_{\text{SAT}}$
854-nm laser detuning	0 MHz
854-nm pulse duration	40 µs
866-nm laser power	15 µW, $\sim 70 \times I_{\text{SAT}}$
866-nm laser detuning	0 MHz
866-nm pulse duration	30 µs

Table 1.1: * With respect to qubit transition frequency.
Experimental parameters used for state preparation of the ion into the $|\downarrow\rangle = |4S_{1/2}, \, m_j = -1/2\rangle$ state.

transitions apart from that needed for state preparation. Figure 1.2 *b*, shows the relevant frequency splitting of the transitions at $\gamma = \pi/2$, which is the set polarisation for all experiments apart from initial quadrupole characterisation. For initial characterisation of the quadrupole transitions, the polarisation was set to $\gamma = \pi/4$, which allowed access to all transitions apart from those forbidden by the beam geometry, $\Delta m_j = 0$, see figure 1.2 *c*.

Other required lasers for manipulating the ion are: the 397-nm and 866-nm lasers used to form a closed-cycle for fluorescence, the 854-nm laser used to deshelve the ion from the $3D_{5/2}$ level for qubit state preparation. Details on these lasers can be found in section A.5.

1.2   Spin

Discrete variable quantum computing consists of manipulating many two-level systems, which we refer to either as spins, or qubits. In this section the methods used to maniplate these spins are described, and their performances are benchmarked.
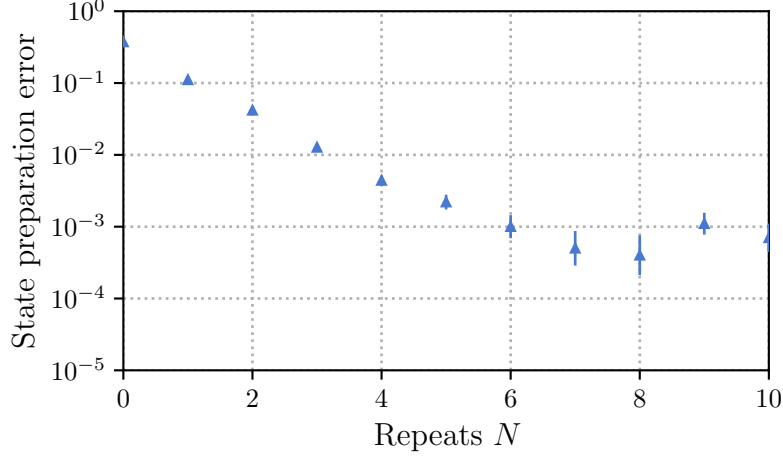
Figure 1.3: State preparation error as a function of the number of state preparation pulses, N. The error is defined as population not in the $|\downarrow\rangle$ state after the preparation sequence has been applied. The error is reduced to below 10^{-3} after $N = 7$ pulses, which is used in our experiments.

1.2.1 State Preparation

To utilise two levels of the ion as a qubit, the electronic state must first be prepared into the qubit manifold. Here, the ion is prepared into the $|\downarrow\rangle = |4S_{1/2},\ m_j = -1/2\rangle$ state. This is done via effective optical pumping by pulsing the quadrupole transition $|4S_{1/2},\ m_j = +1/2\rangle \leftrightarrow |3D_{5/2},\ m_j = -3/2\rangle$, followed by deshelving pulses using the 854-nm, 866-nm lasers on resonance. The 729-nm laser pulse duration and intensity is set to invert the populations, i.e. perform a π-pulse. Details for laser parameters are summarised in table 1.1. These three pulses are repeated N times sequentially. Figure 1.3 shows the state preparation error with increasing N. The error is found by applying a π-pulse on the state preparation transition directly after the state preparation sequence and looking at the population in the $|\downarrow\rangle$ state. Any reduction from $|\downarrow\rangle = 1$ indicates residual population in the $|4S_{1/2},\ m_j = +1/2\rangle$ state, or the D levels. After $N = 7$ pulses, which is used in our experiments, there is a state preparation error of $< 10^{-3}$. This is further verified by randomised benchmarking in section 1.2.3. The state preparation error is likely limited by accidental excitation of the $|4S_{1/2},\ m_j = -1/2\rangle$ state to the $D_{5/2}$ level. This may
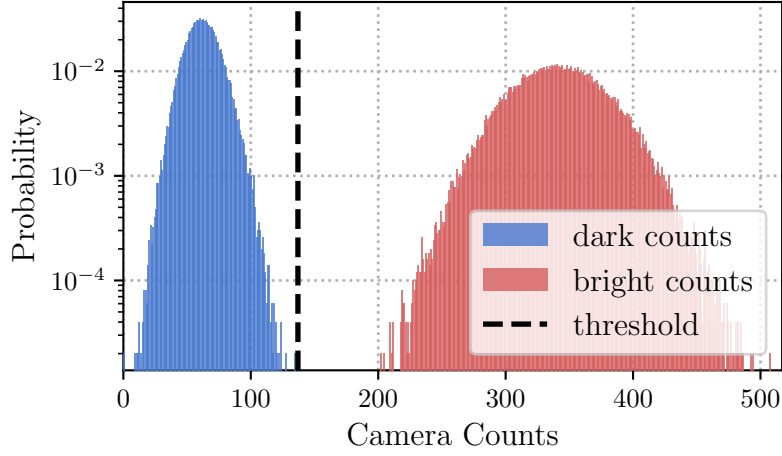
Figure 1.4: Readout histogram with 100,000 individual measurements for bright (red) and dark (blue) populations. The camera counts are presented as a histogram and fitted to Poissonian distributions to calibrate a threshold for discerning if the ion is bright or dark with the lowest probability for false measurement. Dark counts are mainly due to 397-nm light scattered from the nearest trap electrodes. With 100 µs readout duration, and laser parameters set to Doppler cooling parameters, a threshold count of 137 photons is found, giving an expected statistical error of 6×10^{-9} given the fitted Gaussians.

be due to off-resonant excitation of another transition, or due to spectral purity of the 729-nm laser.

Another protocol for state preparation is optical pumping on the dipole transition (397-nm), which often is much faster. However, in this setup it is impractical as polarisation selectivity of the 397-nm transition is not possible due to the constraint of beam geometry from the in vacuum optics, see section A.3, and frequency selectivity is not possible due to the low magnitude fixed B-field providing Zeeman shifts less than the natural linewidth of the 397-nm transition, see section A.2.

1.2.2 Measurement

To measure the qubit state, the 397-nm and 866-nm lasers are applied, and the scattered 397-nm photons are imaged by the objective onto a camera (see section A.4). 397-nm light will only be scattered if the qubit is in $|\downarrow\rangle$. Use of a high numerical aperture (NA = 0.6) objective greatly increases the collection efficiency. This efficiency allows the 397-nm beam to be red-detuned to Doppler cooling parameters

Parameter	Value
397-nm laser power	3 µW, $1 \times I_{\text{SAT}}$
397-nm laser detuning	-17.5 MHz
866-nm laser power	15 µW, $\sim 70 \times I_{\text{SAT}}$
866-nm laser detuning	0 MHz
Doppler cooling duration	1000 µs
Readout duration	100 µs
Camera threshold	137 counts

Table 1.2: Experimental parameters used for Doppler cooling and state-selective fluorescence of the ion.

(see section 1.3.1), while still maintaining low readout duration (100 µs) and low readout error. Cooling during readout increases the experiment's repetition rate by reducing the amount of dedicated cooling time required.

The parameters used for readout are summarised in table 1.2, and a typical histogram of readout counts for one ion can be seen in figure 1.4. The readout threshold is calibrated by taking bright counts with the 397-nm and 866-nm lasers on, and dark counts with the 397-nm laser on and the 866-nm laser off. This assumes dark counts are due to 397-nm scattering from the trap electrodes. Fitting Poissonian distributions to the bright and dark measurements, an optimal count threshold of 137 is found, shown by black dashed line. This threshold gives an expected statistical readout error of $\epsilon_\downarrow = \epsilon_\uparrow = 6 \times 10^{-9}$, where $\epsilon_{\downarrow,\uparrow}$ are the expected error associated with measuring bright or dark. This measurment ignores errors due to the finite lifetime of the metastable $3D_{5/2}$ level, which dominate $\epsilon_\uparrow$. The expected error due to the finite lifetime, τ, is $\epsilon_{\text{decay}} = 1 - e^{-t/\tau}$, where t is the readout duration. For $^{40}\text{Ca}^+$, $\tau \sim 1.1$ s, $\epsilon_\uparrow \approx \epsilon_{\text{decay}} = 10^{-4}$. Assuming the metastable lifetime is limited only by spontaneous decay overlooks leakage from the 854-nm deshelving beam, which could significantly shorten τ [20].

1.2.3 Single Qubit Rotations

A qubit is fully described by $|\psi\rangle = \alpha |\downarrow\rangle + \beta |\uparrow\rangle$, where α and β are complex numbers satisfying $|\alpha|^2 + |\beta|^2 = 1$. The qubit state can be manipulated by applying single
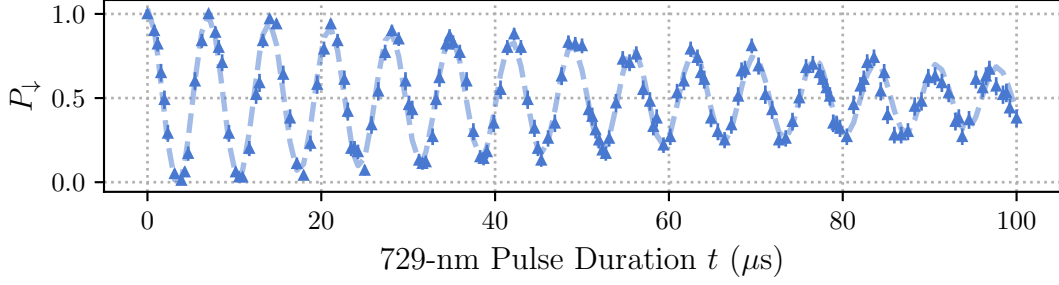
Figure 1.5: Long duration, t, Rabi flop on the qubit transition to extract Rabi frequency. Estimated probability of being in $|\downarrow\rangle$, $P_\downarrow$, at each time step using 200 individual experimental shots. Fitted dotted line using decaying oscillation model. Extracted Rabi frequency $\Omega/2\pi = 0.2864(2)$ MHz, and decay rate $\lambda = 0.0107(7)$ µs^{-1}.

qubit rotations, $R_{x,y}(\theta)$, commonly referred to as gates. In the Bloch sphere, x- and y-rotations are performed by pertubations resonant with the qubit transition, here, using the 729-nm laser. The rotation angle, θ, is given by $\theta = \Omega t/2$, where Ω, is the Rabi frequency, and t is the pulse duration. The rotation axis, is determined by the relative phase of the light field and the qubit. We define the initial relative phase to correspond to a y-rotation.

Gate Time Calibration

The pulse duration, for a $R(\pi/2)$ ($\pi/2$-pulse), is calibrated by Rabi oscillations. Figure 1.5 shows the population in $|\downarrow\rangle$, $P_\downarrow$, calculated from 200 experimental shots. To find the Rabi frequency, Ω, the data is fitted to a decaying oscillation model,

$$P_\downarrow = \frac{1 + e^{-\lambda t}\cos(\Omega t/2)}{2}, \tag{1.1}$$

where λ is the decay rate due to decoherence effects [2]. The Rabi frequency is found to be $\Omega/2\pi = 0.2864(2)$ MHz, and the decay rate $\lambda = 0.0107(7)$ $1/\mu s$. From this $R(\pi/2) = 1.7$ µs can be estimated. These measurements were taken with 1 mW of 729-nm power, with beam radius $\sim$15µm at the ion.
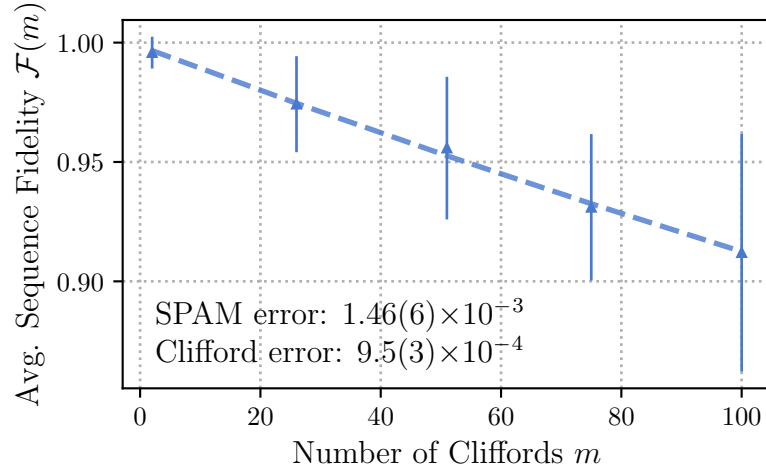
Figure 1.6: Estimating single qubit Clifford fidelities, $\mathcal{F}$, and errors due to state preparation and measurement, using randomised benchmarking. The data points are the average survival population after applying a sequence of m random Clifford gates, and a final inverting Clifford gate. The dashed line is the fit to the decay model given by equation 1.2. The error bars are given by the standard deviation of the survival populations.

Randomised Benchmarking

To evaluate the quality of both our state preparation and single qubit rotations, randomised benchmarking (RBM) [21] is employed. RBM consists of applying random combinations of gates from the single-qubit Clifford group to estimate an average error per gate. The single-qubit Clifford group is the set of unitaries which map the Pauli matrices to one another through conjugation. The RBM protocol used here is described in [22]. The sequence of operations is as follows:

1. Prepare the qubit in $|\downarrow\rangle$ via optical pumping, section 1.2.1.

2. Apply a random sequence of m single qubit Clifford gates, where m is the length of the sequence.

3. Apply a final "inverting" Clifford gate, which is chosen such that the full sequence performs the identity operation.

4. Measure the population in $|\downarrow\rangle$, $P_\downarrow$, via state-selective fluorescence, section 1.2.2.

5. Repeat steps 1-4 multiple times to find the average survival population, $\langle P_\downarrow \rangle$.

6. Repeat steps 1-5 for many different random sequences with a range of sequence lengths, m.

7. Fit the decay of the average survival population, $\mathcal{F}(m) = \langle P_\downarrow(m) \rangle$, to a decay model to find the average error per Clifford gate.

The decay model used to find the fidelity versus number of Clifford gates is given by[22],

$$\mathcal{F}(m) = \frac{1}{2}\left(1 + (1 - 2\epsilon_{\text{SPAM}})(1 - 2\epsilon_c)^m\right), \qquad (1.2)$$

where $\mathcal{F}(m)$ is the fidelity of the sequence of length m, ϵ_{SPAM} is the state preparation and measurement error, and ϵ_c is the average error per Clifford gate. The Clifford gates are decomposed into sequences of $\pi/2$- and π-pulses about either the x- or y-axes. Up to $m = 100$ Clifford gates are probed, and the decay of the fidelity, $\mathcal{F}(m)$, is fit using the above model. The error per Clifford is found to be $\epsilon_c = 9.5(3) \times 10^{-4}$, while the SPAM error is $\epsilon_{\text{SPAM}} = 1.46(6) \times 10^{-3}$. The decay plot for this RBM sequence can be seen in figure 1.6. The independently characterised state preparation (section 1.2.1) and measurement (section 1.2.2) errors of $\sim 10^{-3}$, and $\sim 10^{-4}$ respectively, are consistent with the measured ϵ_{SPAM}.

1.2.4 Spin Coherence Times

Decoherence, as can be seen in figure 1.5, can be caused by laser frequency and power fluctuations, magnetic field noise, and spontaneous emission from the $3D_{5/2}$ level. The coherence time of the qubit is a useful diagnostic for finding unwanted noise sources, and for benchmarking the performance of the qubit as a store of quantum information.

To measure the coherence times, we perform Ramsey sequences with varying delay durations. The Ramsey sequence is as follows:

1. Prepare the qubit in $|\downarrow\rangle$ via optical pumping, section 1.2.1.

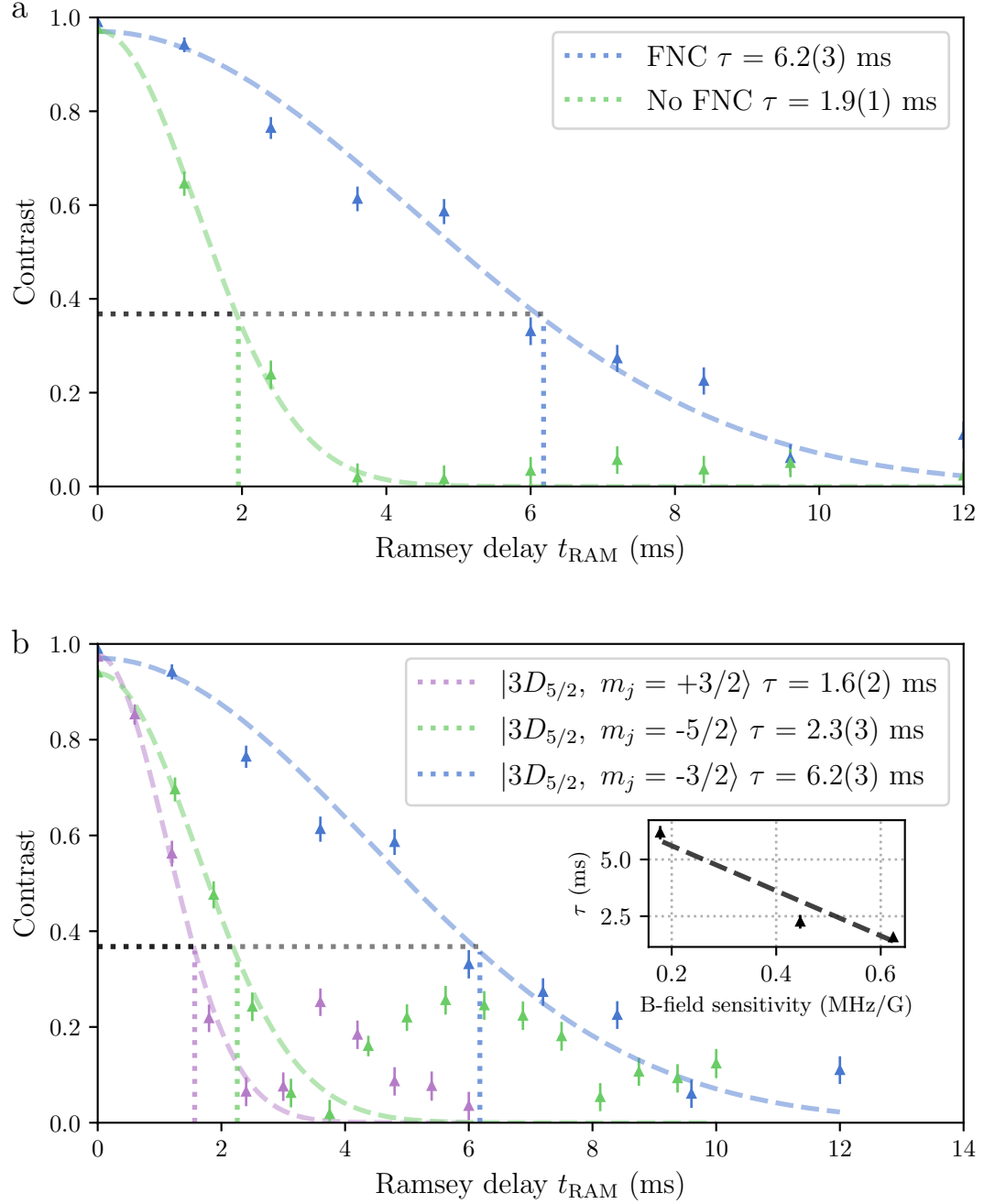**Figure 1.7:** Coherence time measurements. **a)** Coherence time of the $|4S_{1/2}, m_j = -1/2\rangle \leftrightarrow |3D_{5/2}, m_j = -3/2\rangle$ transition with and without fibre noise cancellation (FNC). **b)** Coherence time of three quadrupole transitions with varying magnetic field sensitivities. The inset plot shows a linear fit between the coherence time and the magnetic field sensitivity of the transition.

2. Apply a $R_y(\pi/2)$ pulse to prepare the qubit in $|+\rangle = \frac{1}{\sqrt{2}}(|\downarrow\rangle + |\uparrow\rangle)$ superposition state.

3. Wait for a time t_{RAM}.

4. Apply a second $R_\phi(\pi/2)$-pulse, with a variable axis of rotation, ϕ.

5. Measure the population in $|\downarrow\rangle$, $P_\downarrow$, via state-selective fluorescence, section 1.2.2.

6. Repeat steps 1-5 for different values of ϕ and fit the resulting fringe to find the contrast.

7. Repeat steps 1-6 for different values of t_{RAM} to find the decay in contast with time. The coherence time is defined as the time at which the contrast has decayed to $1/e$ of its initial value.

With this tool, the efficacy of the fibre noise cancellation (FNC, see section A.5.1) can be measured. Figure 1.7 *a* shows the coherence time of the $|4S_{1/2},\ m_j = -1/2\rangle \leftrightarrow |3D_{5/2},\ m_j = -3/2\rangle$ transition with and without FNC. The coherence time is increased from 1.9(1) ms to 6.2(3) ms with FNC, showing that without FNC, the coherence times are limited by laser phase noise.

With FNC enabled, to see if the coherence time is now limited by magnetic field noise, transitions with varying magnetic field sensitivities are compared. Figure 1.7 *b* shows the coherence time of three quadrupole transitions with varying $D_{5/2}$, m_j numbers: $|4S_{1/2},\ m_j = -1/2\rangle \leftrightarrow |3D_{5/2},\ m_j = \{-5/2, -3/2, +3/2\rangle$. These transitions have magnetic field sensitivities -0.446, -0.178, $+0.624$ MHz G^{-1} respectively. The contrast decays for all three qubits are shown in the figure. The inset plot shows a well correlated linear fit between the coherence time and the magnetic field sensitivity, suggesting that the coherence time is limited by magnetic field noise. For both $|4S_{1/2},\ m_j = -1/2\rangle \leftrightarrow |3D_{5/2},\ m_j = -5/2\rangle$ and $|4S_{1/2},\ m_j = -1/2\rangle \leftrightarrow |3D_{5/2},\ m_j = +3/2\rangle$, revivals in contrast can be seen which suggest that the dominant noise source is oscillatory and coherent over the Ramsey scan duration.

These measurements were taken without the MuMetal enclosure (section A.2) fully

assembled around the vacuum system, which we expect will greatly reduce external magnetic field noise, and therefore increase the coherence times.

1.3   Motion

Motion of ions trapped in the same potential can be described by a set of normal modes [23]. These modes are labelled with respect to the ion chain geometry: axial modes oscillate parallel with the chain, and radial modes oscillate perpendicular to the chain. Due to the geometry of the 729-nm beam access with respect to the ion chain (see section A.3), only the radial modes can be addressed in our system. For the *NPL* trap (see section A.1), the radial modes frequencies are non-degenerate. In our system, for a single ion, the radial mode frequencies are $\omega_{\mathrm{upper}}/2\pi = 4.0$ MHz, and $\omega_{\mathrm{lower}}/2\pi = 2.5$ MHz, and the axial mode frequency is $\omega_{\mathrm{axial}}/2\pi = 1.6$ MHz. All work here is using the upper radial mode.

The motional mode, i, leads to sidebands in the 729-nm spectrum at $\omega_0 \pm \omega_i$ [24], where ω_0, the carrier, is the frequency of the 729-nm laser when on resonance with the qubit transition. The $+\omega_i$ sideband is referred to as the blue sideband (BSB), and the $-\omega_i$ is the red sideband (RSB). The RSB, BSB, and RF fields near to resonance with the motional modes, are the tools used in this section to manipulatie the motion of the ion.

The motional state preparation, heating rate, frequency stabilities, and coherence times are characterised in this section.

1.3.1   Cooling

For any interaction that involves the motion of the ion, it is essential to both prepare and measure the motional state with high fidelity. For all motional interactions considered in this thesis, the ion is initially prepared as close as possible to the motional ground state, with a mean phonon number $\bar{n} \approx 0$. This is done by an initial stage of Doppler cooling, followed by pulsed sideband cooling on the 729-nm transition. The final motional state is characterised by measuring the population in

Fock states using RSB and effective BSB pulses.

Doppler Cooling

Doppler cooling relies on the fact that light incident on a moving ion appears frequency-shifted in the ion's rest frame. For Doppler cooling of ^{40}Ca$^+$, both the 397-nm and 866-nm lasers are applied. The 397-nm laser is red-detuned from the dipole $|4S_{1/2}\rangle \leftrightarrow |4P_{1/2}\rangle$ transition, leading to preferential scattering of 397-nm photons that have a net cooling effect [25]. The excited $4P_{1/2}$ level decays via two channels: emission of a 397-nm photon back to $|4S_{1/2}\rangle$, or an 866-nm photon to $|3D_{3/2}\rangle$, with a branching ratio of 14.5 [26]. Since many photon scattering events are required, the cooling cycle must be closed. To prevent population trapping in the metastable $|3D_{3/2}\rangle$ level, the 866-nm laser is applied on resonance during cooling.

Equilibrium is reached when the cooling rate balances photon recoil heating. Assuming the 397-nm transition is broadened only by its natural linewidth γ, the minimum Doppler temperature is,

$$T_{\text{Doppler}} \approx \frac{\hbar\gamma}{2k_B},$$ (1.3)

where $\hbar$ is the reduced Planck constant, and k_B is Boltzmann's constant [25]. For ^{40}Ca$^+$, the natural linewidth of the 397-nm transition is $\frac{\gamma}{2\pi} = 21$ MHz[27], giving $T_{\text{Doppler}} = 0.5$ mK. For a radial mode frequency of $\frac{\omega}{2\pi} = 4$ MHz, the expected mean phonon number is,

$$\bar{n} = \frac{1}{e^{\hbar\omega/k_B T} - 1},$$ (1.4)

yielding $\bar{n} = 2.3$ at the Doppler limit. The parameters used here for Doppler cooling are summarised in table 1.2.
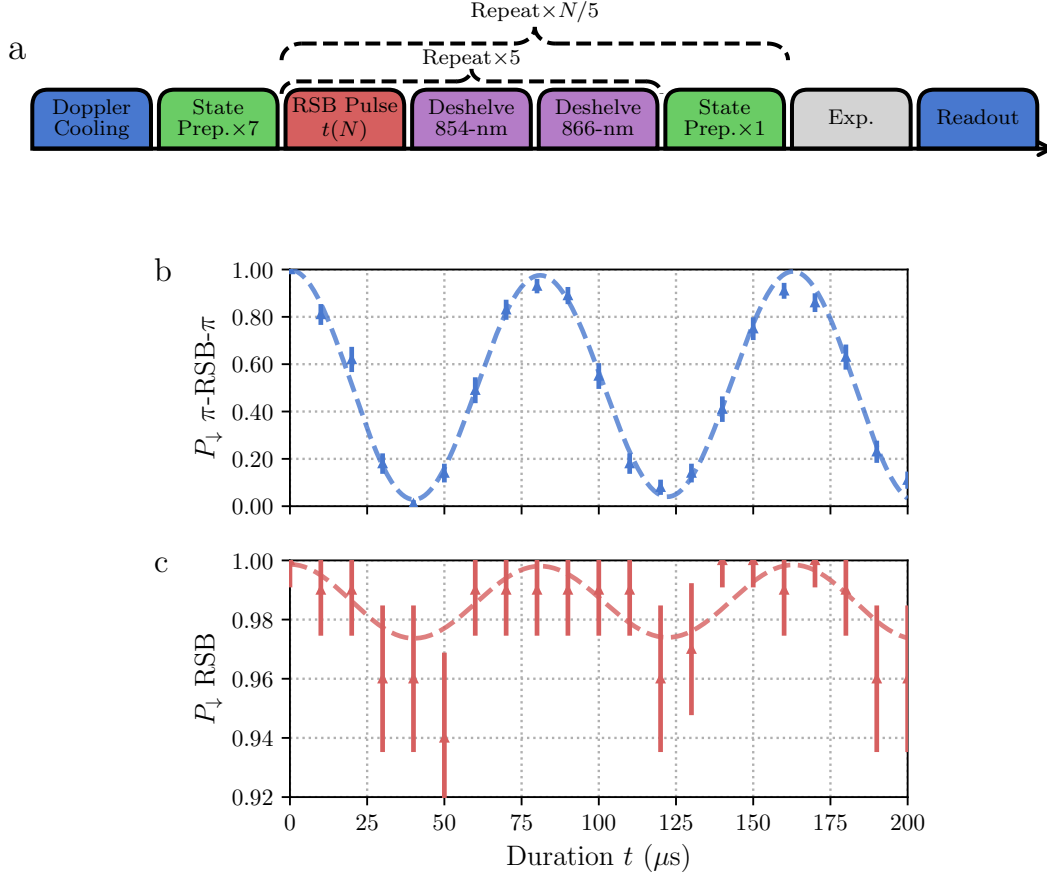
Figure 1.8: a) Example pulse sequence for one experimental shot including pulsed sideband cooling. The *Exp.* block represents an arbitrary sequence of operations, for the experiment under study, such as a thermometry sequence. The blue blocks represent Doppler cooling and readout (section 1.2.2), the green blocks represent qubit state preparation (section 1.2.1), the red blocks are RSB pulses with varying durations $t(N)$, and the purple blocks are deshelving pulses. After every 5 sideband cooling pulses, there is an interleaved state preparation sequence to ensure there is no population trapped outside of the closed cooling cycle. The RSB length is linearly increased with pulse number N, upto the expected RSB $R(\pi)$-pulse duration for $n = 1$. **b, c)** Thermometry scans after Doppler and sideband cooling. The red points are the populations measured via on-resonance RSB pulses, and the blue points are the populations after a sequence of $R(\pi)$-RSB-$R(\pi)$ with varying RSB probe durations. The dashed lines are fits to a thermal Fock state distribution, with truncation at $n = 100$. The extracted mean occupation number is $\bar{n} = 0.03(1)$, and $\eta\Omega/(2\pi) = 11.6(1)$ kHz.

Parameter	Value
729-nm laser power	3.0 mW
729-nm laser detuning	-4.0 MHz*
729-nm pulse duration $N = 1$	2.5 µs
729-nm pulse duration $N = N_{\max}$	33 µs
Repumping 866-nm duration	14 µs
Deshelving 854-nm duration	5 µs
Number of cooling cycles $N_{\max}$	50

Table 1.3: *729-nm detuning is relative to the $|4S_{1/2},\ m_j = -1/2\rangle \leftrightarrow |3D_{5/2},\ m_j = -5/2\rangle$ transition frequency.*
Experimental parameters used for sideband cooling. Other parameters for the repump and deshelve pulses are the same as for state preparation, see table 1.1. The 729-nm laser is detuned to the RSB resonance for the upper radial mode, $\omega_{\mathrm{upper}}/2\pi = 4.0$ MHz, and the pulse duration for $N = N_{\max}$ is chosen to be the expected RSB $R(\pi)$-pulse duration for $n = 1$.

Sideband Cooling

To further cool the ions toward their motional ground state, resolved sideband cooling is used. As mentioned above, the motion of the ion modulates the absorption spectrum of the ion, leading to red and blue sidebands (RSB and BSB). For the $|4S_{1/2}\rangle \leftrightarrow |3D_{5/2}\rangle$ transition, at appropriate motional mode frequencies, interaction strengths, and using a narrow linewidth laser (section A.5.1), these sidebands can be resolved spectroscopically. The pulsed sideband technique employed consists of RSB pulses on the 729-nm transition, followed by deshelving, and repumping pulses on the 854-nm and 866-nm transitions respectively. For efficient cooling, initial short 729-nm pulses are applied to preferentially excite the thermal population with high phonon number, as the pulse duration for RSB $R(\pi)$ is proportional to $\sqrt{n}$, where n is the phonon number. The RSB pulse length is linearly increased to the expected RSB $R(\pi)$-pulse duration for $n = 1$.

An example pulse sequence for a single experimental shot using sideband cooling, can be seen in figure 1.8 *a*. Experimental parameters used are summarised in table 1.3.

To verify the efficacy of our sideband cooling, thermometry experiments are performed by probing Fock state populations. This is done using on resonance RSB
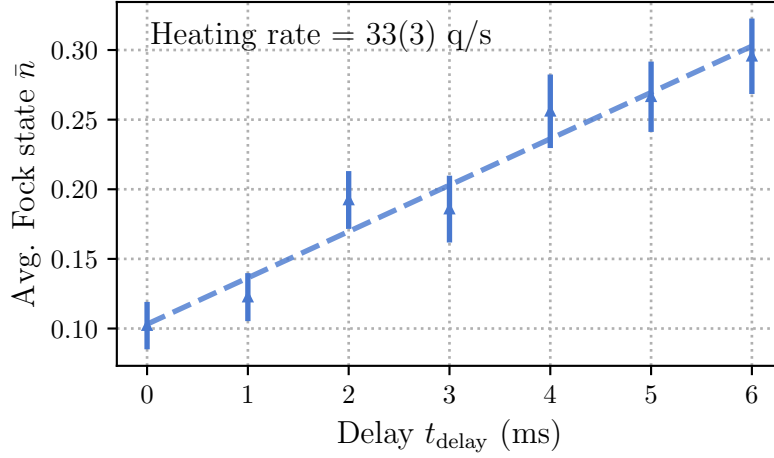
Figure 1.9: Heating rates of upper radial mode, measured by varying the delay between cooling and thermometry pulses. The dashed line is a linear fit to the data, with slope 33(3) quanta/s. The error bars are given by the standard deviation of the fitted $\bar{n}$.

pulses and effective BSB pulses composed of a π-RSB-π pulse sequences. The time dynamics of population flopping is measured as RSB pulse length, t, is varied. In the case of Fock state $|0\rangle$, there should be full contrast "BSB" oscillations, and no visible oscillations when probed with RSB pulses. A thermal Fock state distribution [28] (with truncation at Fock state = 100) is fitted to these signals to extract the mean occupation number, and $\eta\Omega$, the carrier Rabi frequency multiplied by the Lamb-Dicke parameter. A typical thermometry scan after Doppler and sideband cooling can be seen in figure 1.8 b, c, where b shows the population after effective "BSB" pulses, and c shows the population after RSB(t) pulses with duration t. These oscillations are fit to thermal Fock state distributions, shown by the dashed lines. The mean occupation number after sideband cooling is found to be $\bar{n} = 0.03(1)$, and $\eta\Omega = 11.6(1)$ kHz.

1.3.2 Heating Rates

After cooling the motion, the ion will return to a temperature in equilibrium with the environment. However, this process can be slowed by adequate isolation of the ion.

In UHV ion trap systems (see section A.3), motional heating is predominantly caused by electric field noise from the ion trap [2]. Noise due to thermal charge fluctuations at the trap surface can be mitigated by increasing ion-electrode distances. The *NPL* trap (section A.1), used here, has an ion-electrode distance of 250 µm, larger than most surface traps, but less than that of a macroscopic blade or rod style trap [29]. Heating rates were probed by a series of thermometry experiments, explained above, with varying delay times, t_{delay}, between cooling and thermometry pulses. A typical plot can be seen in figure 1.9. The heating rate of the system was found by a linear fit, shown by the dashed line, to be 33(3) quanta per second on the upper radial 4 MHz mode on one ion. As will be discussed in section 1.3.4, the heating rate sets a limit for the motional coherence time.

1.3.3   Motional Mode Stability

Due to thermal drifts and microphonics introducing amplitude and frequency noise on the RF chain, drifts of the radial motional mode frequencies are seen over time. As will be discussed in the following section 1.3.4, this can lead to dephasing of the motional state. Here, the current motional mode stability is characterised to estimate its contribution to dephasing, and to set a benchmark for future stability improvements.

The motional mode frequency is measured via an RF "tickle" experiment. This consists of short (~ 5 µs) RF field pulses applied to one of the trap DC electrodes which has a non-zero electric field projection to the mode we wish to probe. The frequency of the RF field is scanned around the expected motional mode frequency, and when resonant, drives the motion of the ion. This resonance is measured by observing an increase in fluorescence counts using a 397-nm laser red-detuned by 100 MHz. To measure mode frequency drift, this sequence is repeated every 10 seconds over multiple hours. A typical plot can be seen in figure 1.10 *a*. Over this two hour period, the frequency had an absolute drift of 1.5 kHz. Typically, we calibrate the mode frequency every 10 minutes, which is indicated with the red
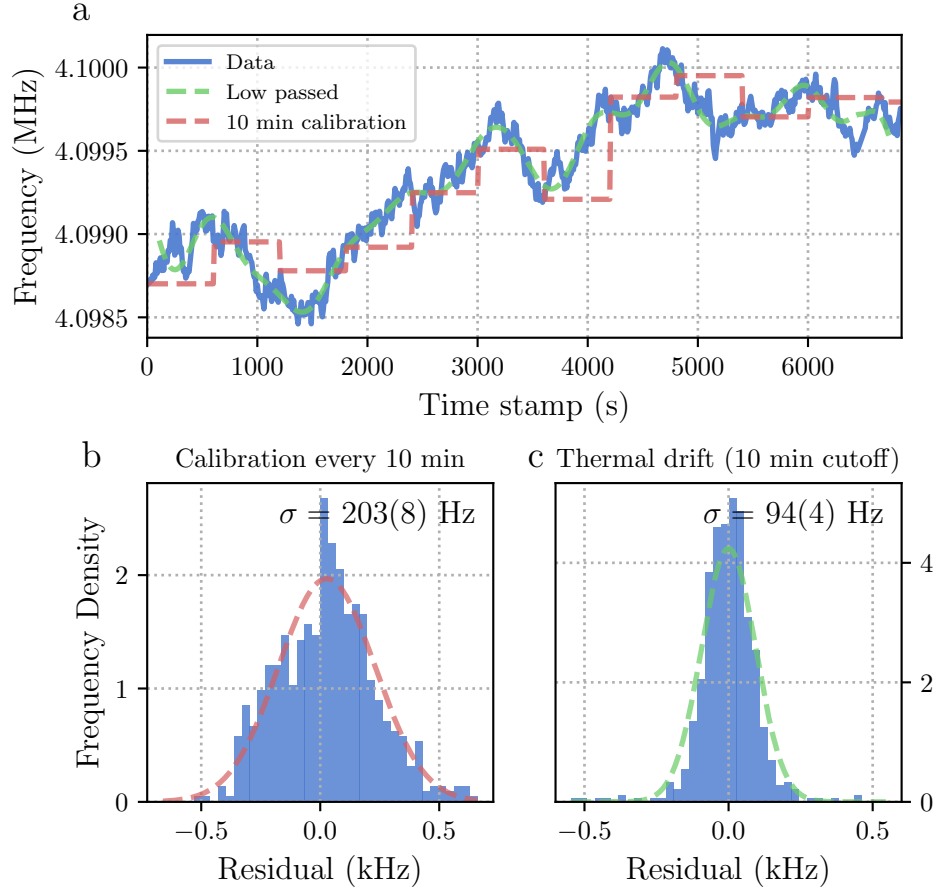
Figure 1.10: a) Motional mode frequency drift over time. The radial motional mode frequency is measured by exciting motion using an RF field in resonance with the motional frequency, and looking at increased fluorescence. The resulting frequency trace is shown in blue. The green line shows a low pass filter of the data, with cut-off frequency of 1.67 mHz, corresponding to an assumed 10 minutes slow thermal drift. The motional mode frequency is typically calibrated every 10 minutes, which is indicated by the red line. **b)** Residuals from the measured data and expected calibrated mode frequencies. The standard deviation of these residuals suggests the typical misset detuning of the mode frequency in current experiments with automated mode frequency calibrations every 10 minutes. **c)** Residuals from the measured data and the low passed trace. The standard deviation of these residuals are due to noise with period less than 10 minutes.
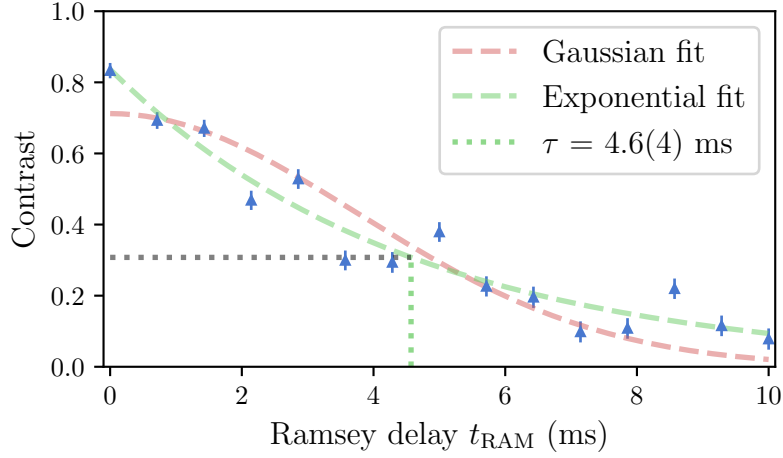
Figure 1.11: Motional coherence time measured by Ramsey sequence on the motional state. The blue points are the population in $|\downarrow\rangle$ after a Ramsey sequence with varying delay time, t_{RAM}. The dashed line is an exponential decay fit, with a coherence time $\tau = 4.6(4)$ ms.

dashed line. Residuals between this calibrated line and the data, shown in b, have a standard deviation of $\sigma/(2\pi) = 203(8)$ Hz, giving the expected uncertainty of the mode frequency detuning given our current periodic calibration routine. A slow drift with frequency cut-off of 1.67 mHz is also fitted to the data, shown in green. The residuals from this fit, shown in c, have a standard deviation of $\sigma/(2\pi) = 94(4)$ Hz. This suggests that the motional mode frequency is relatively stable over time scales shorter than 10 minutes, but has a slow drift on longer time scales, which is likely due to thermal fluctuations.

1.3.4 Motional Coherence Times

We will utilise the motional modes of the ion to store quantum information. As with the section on spin coherence times 1.2.4, the fidelity of operations, and success probability of algorithms will be limited by the coherence time of the motional state. To measure motional coherence, a Ramsey sequence is performed between states $|\downarrow, 0\rangle$ and $|\downarrow, 1\rangle$, where the first element is the qubit state, and the

second element is the motional Fock state. To prepare these states the following pulse sequence is applied:

1. State prepare system to $|\downarrow, 0\rangle$ via optical pumping and sideband cooling.

2. Apply $R_y(\pi/2)$-pulse on carrier transition to prepare the qubit in $(|\downarrow, 0\rangle + |\uparrow, 0\rangle)/\sqrt{2}$.

3. Apply $R(\pi)$-pulse on the RSB to prepare the motional state in $(|\downarrow, 0\rangle + |\downarrow, 1\rangle)/\sqrt{2}$.

4. Delay for some time t_{RAM}.

5. Apply $R(\pi)$-pulse on the RSB to map accumulated phase onto the qubit state.

6. Apply $R_\phi(\pi/2)$-pulse on the carrier, with variable axis of rotation, ϕ.

7. Measure the population in $|\downarrow\rangle$ via state-selective fluorescence, section 1.2.2.

8. Repeat steps 1-7 for different values of ϕ to find the contrast of the Ramsey fringe.

9. Repeat steps 1-8 for different values of t_{RAM} to find the decay in contrast with time. The coherence time is defined as the time at which the contrast has decayed to $1/e$ of its initial value.

There are two main mechanisms for motional decoherence[30]: motional heating, as characterised in section 1.3.2, and motional dephasing due to mode frequency instability, as discussed in section 1.3.3.

A heating rate dominated coherence time is given by, $\tau_{\text{HEAT}} = (\sqrt{e} - 1)/\dot{\bar{n}}$ [30], where $\dot{\bar{n}}$ is the heating rate. A dephasing dominated coherence time, if noise is correlated on timescales long compared to the Ramsey delay [31], is characterised by a Gaussian decay profile with a coherence time of $\tau_{DEPH} = \sqrt{2}/\sigma_\omega$.

Evaluating both of these models with $\dot{\bar{n}} = 33(3)$ q/s, and $\sigma_\omega/(2\pi) = 94(4)$ Hz, the expected motional coherence times of $\tau_{\text{HEAT}} \approx 20$ ms and $\tau_{\text{DEPH}} \approx 2.3$ ms respectively, are found. From these auxiliary characterisations of the motional

modes, it is expected that the coherence time will be limited by motional dephasing. Figure 1.11 shows the decaying coherence when probed by the above sequence. It can be seen that the contrast has a good fit assuming an exponential decay (green dashed line), defined by $C(t_{\mathrm{RAM}}) = C(0)e^{-t_{\mathrm{RAM}}/\tau}$, where $C(t_{\mathrm{RAM}})$ is the contrast at time t_{RAM}, and τ is the coherence time. The fit yields a motional coherence time of $\tau = 4.6(4)$ ms, defined as the time at which the contrast decays to $1/e$ of its intitial value. An exponential decay suggests that the noise source causing the dephasing is correlated only for durations much shorter than the Ramsey delay times [31]. The Gaussian decay, (red dashed line), which was appropriate for the previous spin coherence time measurements in section 1.2.4, is a poor fit here.

1.4   Spin-Motion

For full control of the spin-motion hybrid system, we require interactions that couple the two. Perhaps the simplest of this class of interactions are the red- and blue-sidebands (RSB and BSB respectively). The RSB interaction was used previously in the thermometry and sideband cooling sections 1.3.1. The RSB (BSB) consists of a single frequency laser tuned at the carrier frequency minus (plus) the motional mode frequency, ω_m. The interaction is well described by the (Anti-) Jaynes-Cummings Hamiltonian, and effectively couples spin flips with the addition or subtraction of a motional quanta depending on the initial spin state. Here, another such interaction coupling spin and motion, known as the spin-dependent force, SDF, is introduced. While the RSB and BSB interactions couple the spin and motion in the motional Fock basis, the SDF couples them through spin-dependent displacements, thus in a coherent state basis. The direction of the displacement is determined by the spin state and an effective detuning parameter.

1.4.1   Spin-Dependent Forces

The optical Mølmer-Sørensen (MS) scheme [6] is used to generate the SDF via a bichromatic laser field. Bichromatic refers to the simultaneous application of two

tones symmetrically detuned around the qubit carrier frequency, with absolute detuning approximately equal to the motional mode frequency, $\delta \approx \omega_m$. The resulting interaction, when ignoring off-resonant and higher order couplings, is given by,

$$\hat{H}_{MS} = i\hbar\eta\Omega\hat{\sigma}_\phi \cos(\delta t)\left(\hat{a}e^{-i\omega_m t} + \hat{a}^\dagger e^{i\omega_m t}\right), \tag{1.5}$$

where η is the Lamb-Dicke parameter, Ω is the carrier Rabi frequency, $\hat{a}(\hat{a}^\dagger)$ is the lowering (raising) operator, and $\hat{\sigma}_\phi$ is the Pauli operator with $\hat{\sigma}_\phi = \cos(\phi)\hat{\sigma}_x + \sin(\phi)\hat{\sigma}_y$. Applying the rotating wave approximation, and defining $\delta_g = \delta - \omega_m$, the interaction Hamiltonian can be approximated to,

$$\hat{H}_{MS} \approx \frac{i\hbar\eta\Omega}{2}\,\hat{\sigma}_\phi\left(\hat{a}e^{-i\delta_g t} + \hat{a}^\dagger e^{i\delta_g t}\right). \tag{1.6}$$

The trajectory of this displacement can be controlled by varying δ_g: on resonance, $\delta_g = 0$, corresponds to linear trajectories, whilst off resonance, $\delta_g \neq 0$, corresponds to cyclic trajectories where after some duration $t = 2\pi/\delta_g$, the motion returns to the initial state (with perhaps some phase shift [32]). The dynamics of the SDF may be measured by projective spin measurements, the population in $|\downarrow\rangle$, $P_\downarrow$, after applying the SDF for duration t is described by [33],

$$P_{\downarrow,\text{th}} = \frac{1}{2}\left[1 + e^{-4\left(\bar{n}+\frac{1}{2}\right)|\alpha(t,\delta_g)|^2}\right], \tag{1.7}$$

where $\bar{n}$ is the initial thermal phonon occupation, and $|\alpha(t,\delta_g)| = \Omega_{\text{SDF}}\sin(\delta_g t/2)/\delta_g$, is the absolue displacement of the initial state. This control is utilised in both two-qubit entangling gate experiments, as well as in the creation of squeezed states.

Calibrating the SDF

Geometric phase gates, such as the MS interaction, are widely employed in ion trap experiments due to their robustness against variations in initial motional state. However, the SDF is sensitive to various frequency and power miscalibrations and drifts of these between calibrations. Here, we describe the workflow for calibrating and optimising the SDF behaviour.
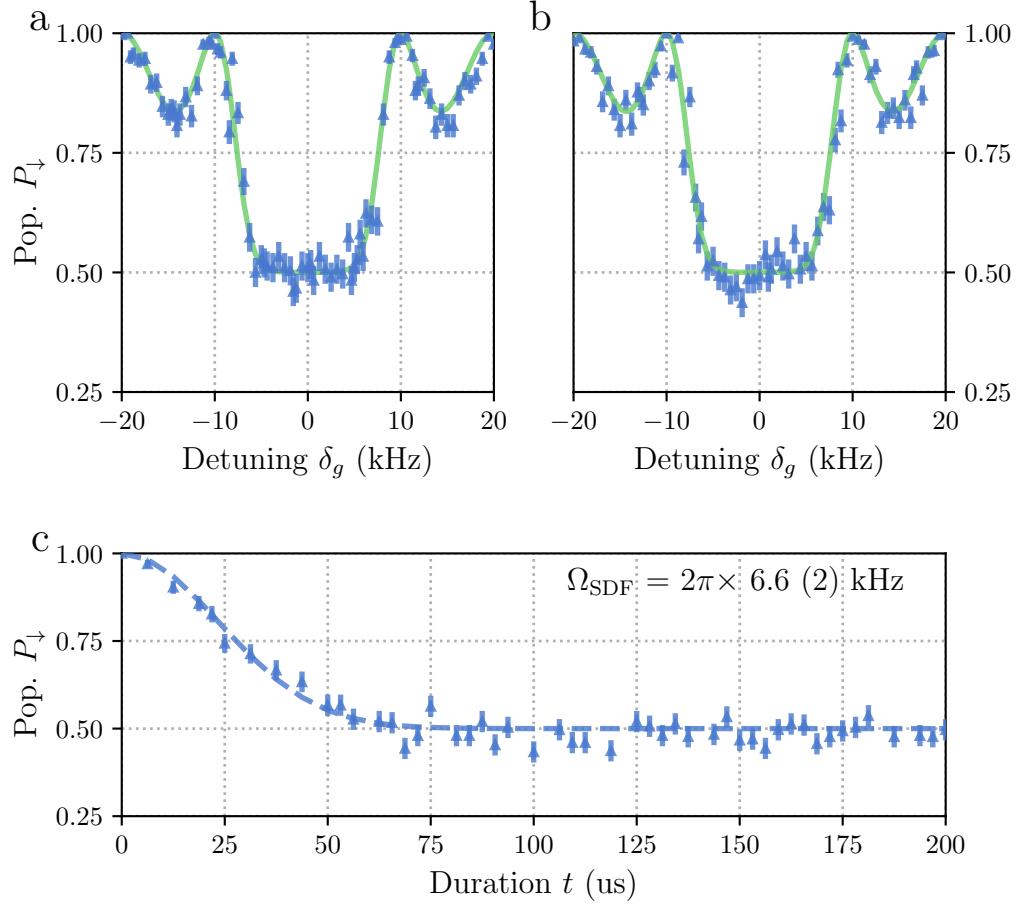
Figure 1.12: Detuning and duration scans of the spin-dependent force applied to an initial thermal state with $\bar{n} = 0.03(1)$. **a)** Detuning scan, where the detuning, δ_g, is varied, and the duration is fixed at $t = 100$ µs. The green line is a fit to the expected behaviour given by equation 1.7. **b)** Detuning scan with a misset qubit frequency of 0.5 kHz. The green line is the same fit as in a to guide the eye. **c)** Duration scan, where the duration, t, is varied, and the detuning is fixed at $\delta_g = 0$. The dashed line is a fit to the expected behaviour given by equation 1.7 with only Ω_{SDF} as a free parameter.

In practice, the SDF interaction involves relatively few degrees of freedom: the central qubit frequency, the motional mode frequency, the power in each tone, and the durations of the pulses must all be calibrated. The complexity comes from the fact that the ion is a multi-level system, posseses multiple motional modes, and that each experimental parameter can only be controlled with finite precision.

The effect of nearby motional modes is negated by either selecting the interaction mode to be well seperated from the others either in frequency, by beam geometry, by operating the SDF near to resonance of the desired mode, or by using amplitude shaping of the pulse. Smoothing a square pulse through amplitude shaping narrows the pulse frequency bandwidth, and thus reduces unwanted off-resonant excitation of other modes.

The power balance of the SDF tones is complicated due to our use of AOMs. AOMs generate frequency shifts in the laser beam at the expense of small frequency-dependent angular shifts. After the AOM, the beam is coupled into a single mode fibre (see figure A.4), and so the AOMs effectively introduce a frequency-dependent loss. To calibrate the power balance, a pick off of the bichromatic beam after the ion is monitored on a high bandwidth photodiode. The beatnote contrast is measured for the two tones and the power balance is optimised by maximising this contrast.

The far off-resonant levels of our ion lead to light-shifts of our qubit frequency. To account for the light-shift the central qubit frequency must be calibrated at the optical power used for the interaction. This is done with the SDF interaction itself. When the qubit frequency is set incorrectly, the two tones will no longer have the same absolute detuning from their respective RSB or BSB. This manifests as a "skewness" of the SDF detuning trace. By varying the qubit frequency and inspecting these detuning scans, the desired SDF behaviour can be found.

To verify the behaviour of the calibrated SDF, the experimental data is compared with theory. Both "detuning" and "duration" scans are used. The "detuning" scan is performed by varying the detuning, δ_g, of the interaction, whilst keeping the SDF duration, t, constant, and vice-versa for the "duration" scan.

Figure 1.12 c shows the measured duration scan described by equation 1.7, with

$\delta_g = 0$ and the the motional state assumed to be thermal with average Fock state $\bar{n} = 0.03(1)$ which was found previously from thermometry measurements. Here, the displacement, $|\alpha(t)| = \Omega_{\text{SDF}} t/2$, where Ω_{SDF} is the SDF amplitude. The dashed line fit is given by floating Ω_{SDF} only, and finds $\Omega_{\text{SDF}}/(2\pi) = 6.6(2)$ kHz. These measurements were performed with total 729-nm power of 2 mW and $\delta_{\text{LS}}/(2\pi) = 3.5$ kHz, the light shift due to the 729-nm laser relative to the unperturbed qubit frequency.

The detuning scan, shown in figure 1.12 *a*, has the same experimental parameters, but with fixed duration $t = 100$ us. The fit in green is taking the displacement to be $|\alpha(t)| = \Omega_{\text{SDF}} \sin(\delta_g t/2)/\delta_g$, given the value for Ω_{SDF} measured from the duration scan. Here, a qualitatively good agreement between the measured data and the expected behaviour is seen, with the main features being the "closure" at $\delta_g = 2\pi/t$ where the motional state returns to the initial state, and the central flat region around $P_{\downarrow,\text{th}} = 0.5$ where the two motional wave packets are non-overlapping. Figure *b* shows an example detuning scan when the qubit frequency is misset by 0.5 kHz. The central region now displays a clear assymmetry around $\delta_g = 0$. The green line here is the fit from *a* to guide the eye.

1.4.2   Two-Qubit Entangling Gates

We perform two-qubit entangling gates using the Mølmer-Sørensen (MS) interaction [6]. This interaction is the same described SDF from the previous section, but applied globally to two ions. The MS interaction relies on the spin dependent geometric phase accumulated during the motional displacement [24]. To create a two-qubit entangled state, a differential geometric phase of $\pi/2$ must be accumulated between the two-qubit basis states [24]. To ensure there is no residual motional entanglement, the final motional state must return to the initial state. In practise, using an SDF detuned by δ_g, this is achieved by applying the MS interaction for a duration $t_g = 2n\pi/\delta_g$, where n is the number of "loops". The MS gate is a universal two-qubit gate, and along with only single qubit gates, constitutes a universal gate set for discrete quantum algorithms.
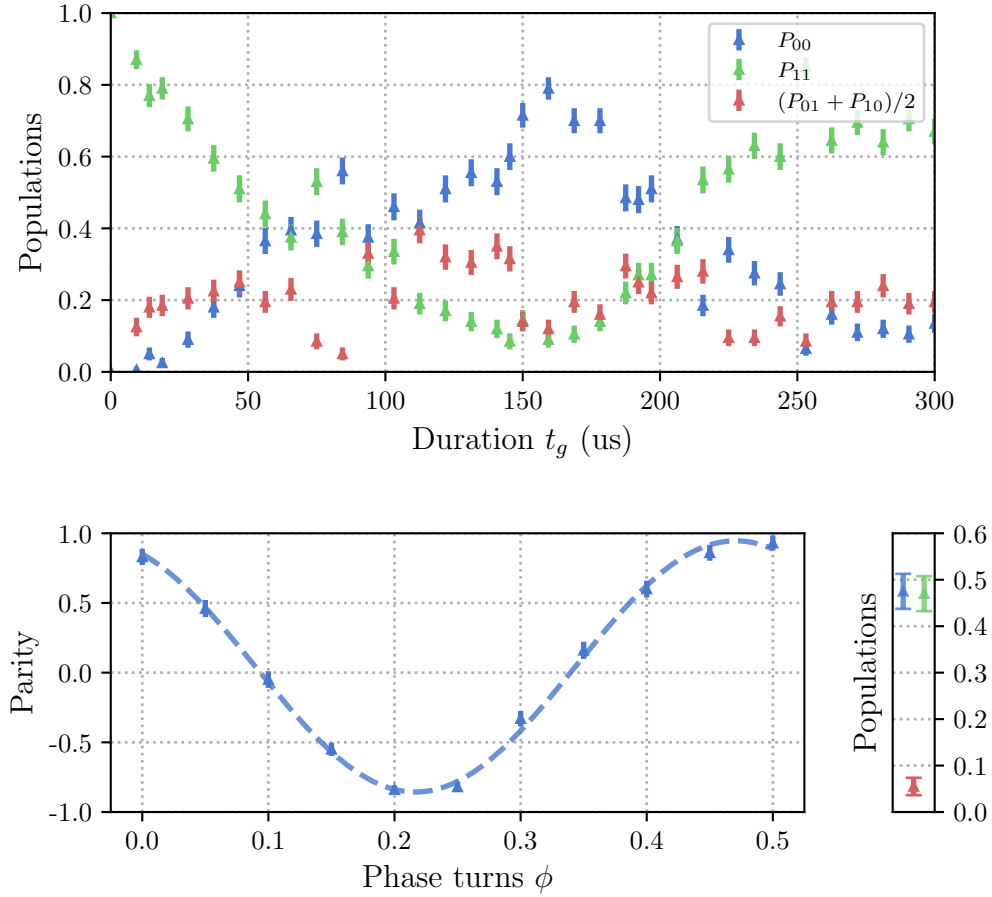
Figure 1.13: Experimental data for $\mathcal{F} = 92(2)\%$ Mølmer-Sørensen (MS) two-qubit entangling gate. **a)** Populations versus duration scan of the MS interaction. Each point corresponds to the average of 200 shots, and the error bars are given by the standard deviation of these averages. The blue points are the populations of both ions being in the $|0\rangle$ state, P_{00}, the green points are the populations of both ions being in the $|1\rangle$ state, P_{11}, and the red points are the ions being the the opposite states, $(P_{01} + P_{10})/2$. The desired entangling gate corresponds here to $t_g = 75\mu s$. **b)** Parity oscillations after the MS interaction. The parity is defined as $P_{00} + P_{11} - P_{01} - P_{10}$. The fitted contrast here is $0.90(2)$. **c)** Populations at the desired entangling gate duration, $t_g = 75$ us.

Here we quote the current fidelity of experimentally demonstrated two-qubit gates on our system. The fidelity serves to quantify the similarity of two density matrices. Here for a two-qubit entangling gate, we target the creation of the Bell state $|\Phi^+_{\phi_0}\rangle = 1/\sqrt{2}\left(|00\rangle + e^{i\phi_0}|11\rangle\right)$, from an initial state of $|00\rangle$, where phi_0, is some fixed phase. The fidelity between our mixed state ρ, and the pure Bell state may be given by,

$$\mathcal{F} = \langle\Phi^+_{\phi_0}|\,\rho\,|\Phi^+_{\phi_0}\rangle = \frac{1}{2}\left(\rho_{00,00} + \rho_{11,11}\right) + \frac{1}{2}\left(e^{i\phi_0}\rho_{11,00} + e^{-i\phi_0}\rho_{00,11}\right), \qquad (1.8)$$

where $\rho_{ij,kl} = \langle ij|\rho|kl\rangle$. To extract the fidelity experimentally, a partial state tomography protocol is used [34], where the first bracketted term of equation 1.8 is measured by performing projective measurements of the two ions after the gate sequence to extract populations, and the second bracketted term, known as the coherence terms, are measured by applying a global analysis $R_\phi(\pi/2)$ pulse to the two ions and applying parity measurements. Parity measurements are defined as $P = P_{00} + P_{11} - P_{01} - P_{10}$, where P_{ij} is the population of the two ions in state $|i\rangle\,|j\rangle$ after the gate sequence and variable $\pi/2$-pulse. Creating a Bell state is essential for two-qubit entanglement, but its basis can vary as long as it is consistent across experiments. This allows the Bell state phase, ϕ_0, to float, which in practice means using only the amplitude of the fitted parity oscillations to compute fidelity, ignoring any phase offset.

The best two-qubit entangling gate fidelity currently achieved on our system is $\mathcal{F} = 92(2)\%$. As shown in figure 1.13, the magnitude of the parity scan was measured to be $0.90(2)$, while the populations $(\rho_{00,00} + \rho_{11,11}) = 0.95(2)$. Each population point in these figures are found by taking the average of 200 shots of the gate sequence.

These results serve as both a proof of principle for full spin control on our system, but also as a benchmark to which we can compare future system improvements. For future work, we will require the use of this entangling gate either as Bell state preparation for input to analogue simulation experiments [35], or as a primitive gate for the spin component of hybrid algorithms [11, 12]. In both these cases,

especially any use that requires multiple concatenated entangling gates, we will likely require improved gate fidelities. Current gate fidelities are limited by the motional dephasing. The gate error due to motional dephasing follows (see section 4.4.6 [36])

$$\epsilon_{\text{DEPH}} = 0.686 \frac{t_g}{\tau_{\text{DEPH}}}, \tag{1.9}$$

where for these experiments we estimate a motional coherence time of approximately $\tau_{\text{DEPH}} = 1$ ms. Given the gate duration of $t_g = 75$ µs, this gives a dephasing error of $\epsilon_{\text{DEPH}} = 0.05$, or approximately 5%. This is the dominant error source in our current gate fidelity, and can be improved by decreasing the gate duration, or by improving the mode frequency stability. We have not yet attempted to optimise these gates, nor have we attempted to fully account for the observed errors. However, this work serves as a benchmark for future improvements, and a demonstration of the full spin control capabilities of our system.

Appendices

A

Ion Trap Apparatus

Contents

A vast effort is spent on the initial build-up of the ion trap system, but throughout the life of the experiment, a greater effort is spent on its daily maintenance. I hope that this chapter will serve as a useful debugging-resource for future members of the FastGates team, and as a detailed recipe for anyone building a similar system.

Due to the size and complexity of the system, in this chapter we introduce an overview of the design, motivated by the desired functions. Many such ion trap experiment overviews exist in the theses of previous PhD generations, and so we will limit the discussion here to the unique features and capabilities of our system. As a map for this section we state the landmark features of an "ion trap" experiment.

First, to confine the ions, static and dynamic electric fields are used which, due to ions possesing non-zero electric charge, can provide trapping potentials, section A.1. Due to the fragility of the internal states of the ion (these are state -of-the-art sensors after all), we must take great care in isolating the ion from any noisy environment. This neccesitates the use of ultra-high vacuum (UHV) systems, section A.3, vibration isolation, and magnetic shielding, section A.2. To manipulate the internal electronic states of the ion, local electric and magnetic fields are created using RF antennae and, in this work, lasers, sections A.5 and A.5.1. Finally, to interface with the apparatus we have built, at the time scales set by our interaction strengths, we require a sophisticated and custom control system.

A.1 The Ion Trap

From Earnshaw's theorem, $\nabla^2 V = 0$, a stable stationary point in 3D cannot be realised using only static electric potentials, V, as if the potential is confining in two dimensions, it will be anticonfining in the third. Therefore, to achieve stable trapping, either an oscillating electric field (Paul trap [38]), or a static magnetic field (Penning trap) is used.

Recently, the microfabricated surface style linear Paul trap has gained popularity due to the maturity of chip fabrication technologies [39] and the potential route to scalability this offers [40]. In the surface trap, the 3D radial and axial electrodes of a "macro" trap are effectively projected onto a 2D surface. The stable confining point of such a trap is typically on the order of $50 - 100$ μm above the chip surface. The ease of fabrication of surface traps has allowed the creation of complex multizone devices with many DC electrodes. These multizone traps enable the shuttling of ions, a requirement for Quantum CCD type architectures [40]. However, this surface style geometry typically comes with two costs: the depth of the trapping potential is often greatly reduced, and the close proximity of the surface to the ion can be a large contributor to motional heating rates [2, 41].

Our trap is provided by the *National Physical Laboratory* in the UK. This is a microfabricated 3D trap, which brings together the advantages of chip fabrication
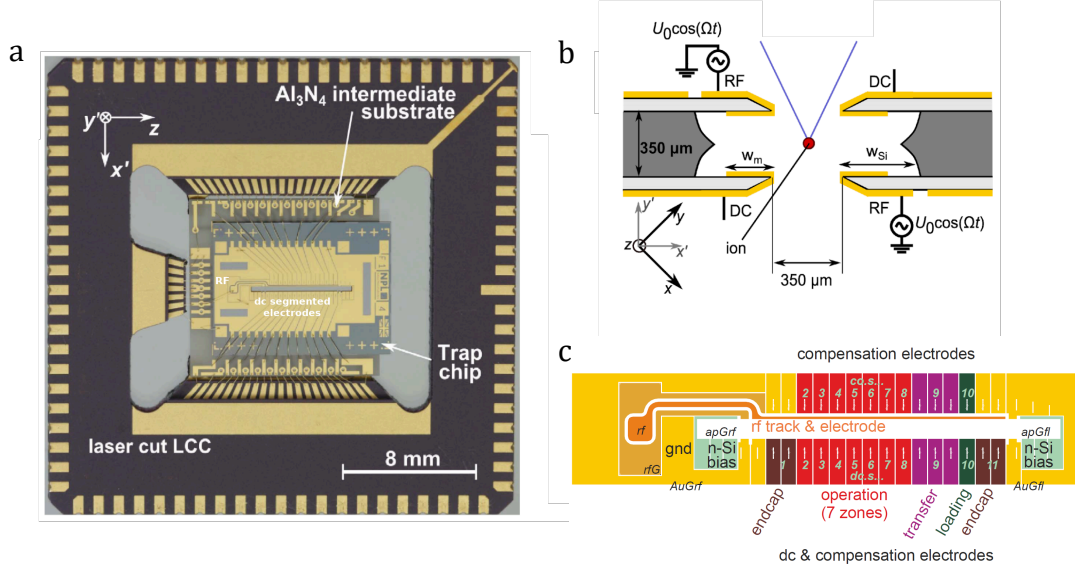
Figure A.1: Schematics of the *NPL* trap chip used in this experiment. **a)** A front view of the trap chip. Axial confinement is provided by a subset of the segmented DC electrodes. Radial confinement is provided by the RF rails. **b)** A slice view of the trap. The red point here represents the ions, the gold are the RF and DC electrodes, and the grey is the silica substrate. It can be seen that the ion is $\sim 250\mu$m away from the nearest electrode. The numerical aperture of the ion due to the electrodes is ~ 0.71. **c)** A schematic of the electrode geometries and labelling for the front-face of the trap chip. A similar arrangement exists for the back-face. Figures from [37].

as well as the low heating rates and high trapping depths of a 3D style trap with greater ion-surface distances. Details on its design and characterisations can be found in [42, 43]. Figure A.1 shows the electrode geometry of the trap and the relevant length scales. The ion-surface distance is now of the order 250 μm and we have demonstrated heating rates of 33(3) q/s on a 4 MHz radial mode (see section 1.3.2).

An axial ion separation of ~ 5 μm is desired. For ^{40}Ca$^+$ ions this means an axial mode frequency of $\omega_z \approx 2\pi \cdot 1.6$ MHz. This ion separation was chosen as a balance between the desire for high mode frequencies while keeping cross talk due to laser-addressing negligible.

The mode frequencies that can be achieved are ultimately limited by the breakdown

voltage of the trap electrodes, $V_{\text{MAX}} = 400$ Vpp. Within this constraint, we are targeting ~ 4 MHz for our radial frequencies. The choice of this higher frequency is motivated by several factors: the Doppler cooling limit is reduced, and the frequency separation between modes can be increased, which is useful for simplifying interactions involving motion.

In the following two sections we describe the experimental parameters used in our apparatus to achieve these mode frequencies.

A.1.1 Trap RF Chain

To utilise radial motional modes for low error quantum gates, we require the radio frequency (RF) field that produces the desired trapping pseudopotential to be both frequency and amplitude stable. Our *NPL* trap is rated for a max peak-to-peak voltage of 400 Vpp on the RF electrodes. Here we describe the elements of the "RF chain" that supplies this voltage.

Our frequency source is a DDS-based synthesiser, named *Urukul*, part of the *Artiq Sinara* [44] hardware ecosystem. The *Urukul* is operated at maximum output power, +10 dBm, and with a frequency ~ 27.8 MHz. This signal is then fed to an "ultra-low noise limiting amplifier" named *Squareatron*. The purpose of *Squareatron* is to greatly reduce the amplitude noise of the RF signal, V_{RF}, which is key to low radial mode frequency drifts, as radial mode frequency $\omega_{x,y} \propto V_{\text{RF}}$ [2]. The *Squareatron* outputs +17.4 dBm, which is subsequently attenuated by 19.5 dB. The signal is then amplified by a further 33.7 dB using a *Mini-Circuits ZHL-1-2W-S+*, high power amplifier. The signal is now +32 dBm RF power, enough to drive the trap electrodes. To impedance match the 50 Ω line from the amplifier to the small capacitance (~ 5 pF) of the trap electrodes, an LC impedance matching circuit is used. This LC circuit has a tuned resonant frequency of 27.84 MHz, and a measured Q factor of 43.8 found using a vector network analyser and fitting S11 impedance measurements. This resonant matching circuit has three main effects: it ensures good power transfer between RF input and trap electrodes via impedance matching,

it steps up the voltage to the required 400 Vpp, and it filters out RF noise and unwated harmonics due to the narrow bandpass nature of the LC circuit.

If components are chosen well, and adequately protected from environmental noise, this chain can produce the desired frequency and amplitude stable RF. Characterisations of the motional mode stability are discussed in section 1.3.3. We are still yet to fully quantify and debug the motional stability against thermal and mechanical noise, however it should be noted that other groups do opt for active stabilisation of RF amplitude through closed feedback loops [29].

A.1.2 Trap DC Voltages

Voltage is supplied to the 40 DC electrodes using *Fastino*, a multi-channel DAC part of the *Artiq Sinara* hardware ecosystem.

The ion is confined in the "operation" zone, seen in figure A.1 c. The axial trapping is provided by electrodes DC-b5 and DC-f5, where b and f correspond to the back and front plane of the trap. The DAC provides ~ 10 V to these electrodes to produce an axial frequency of 1.6 MHz.

A.2 Magnetic Field

Stable Zeeman shifts of the ion energy levels are required for long spin coherence times (see section 1.2.4), and for low error single- and two-qubit gates. A permanent magnet array of Samarium Cobalt, Sm_2Co_17, is used in a Helmholtz configuration to create a stable magnetic field of 5.4 G. Samarium Cobalt was chosen for its low temperature coefficient of remanence, -0.03%/K.

The ion is shielded from unwanted external magnetic fields by two layers of 3 mm thick MuMetal shielding from *MagneticShields*. The factory quoted shielding factor is 546 for DC fields. Spin coherence time comparisons for the ion with and without magnetic shielding are shown in section 1.2.4.
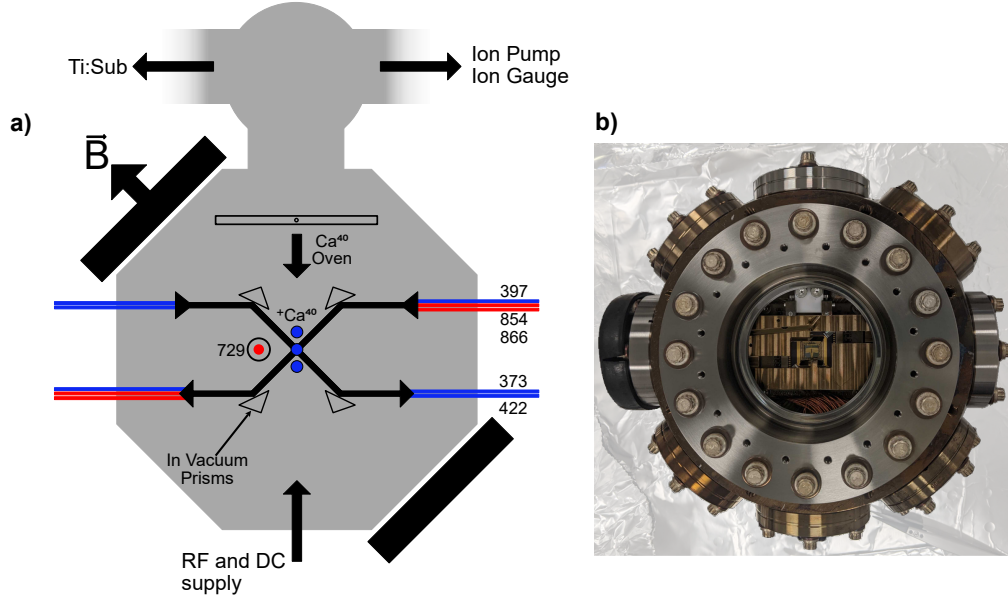
Figure A.2: a) A schematic of the vacuum chamber. Wavelengths apart from 729-nm enter through the side CF40 viewports and are directed onto the ions by in vacuum prisms. The 729-nm light enters through the larger CF100 viewports. **b)** A photograph of the assembled system prior to baking.

A.3   Vacuum System and Beam Geometry

Ultra High Vacuum (UHV) is required to extend the ion storage lifetime. However, UHV equipment is often bulky, and puts constraints on the access and visibility of the ion chain. Here we describe the designed vacuum system, and beam access. The vacuum system and beam geometries were designed by Sebastian Saner and Mariella Minder, and constructed by Sebastian Saner, Fabian Pokorny, and myself. A residual pressure of $< 10^{-11}$ mbar is desired. For this strict requirement, care must be taken in selecting in-vacuum materials, and thorough cleaning and baking procedures must be followed. A summary of tactics that were useful in the construction of the vacuum system can be found in [45, 46].

A schematic and photograph of the vacuum system can be seen in Figure A.2. The system consists of a 6" spherical-octagonal experimental chamber[1] connected to a spherical chamber with ion pump[2], ion gauge[3] and Titanium sublimator

---

[1]Kimball MCF600-SphOct-F2C8

[2]Agilent VacIon Plus 20 Pump
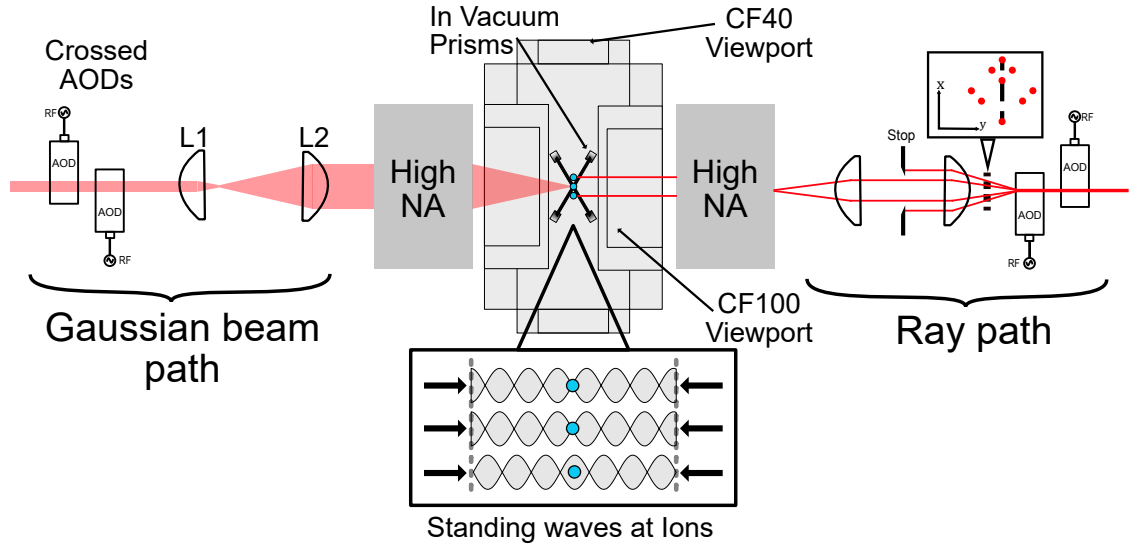
[3]Agilent UHV-24P Ion gauge

Figure A.3: The standing wave single addressing system. Dual high NA objectives focus the light to a tight waist at the ions location. AODs are used to steer the light to only selected ions. The left hand side of the figure shows the Gaussian profile of the light, whilst the right hand side shows a ray representation of how two singly addressing spots are formed at the ions. L1 is a telecentric scanning lens and in combination with L2 form a beam expander.

pump (TSP)[4] attached. The ion pump and TSP maintain the UHV to the desired $< 10^{-11}$ mbar. We find that on the ion pump alone UHV cannot be maintained indefinitely, however, firing the TSP every 4 weeks with 41 A for 60 seconds provides a sufficient pumping rate. At the time of system baking, a He leak test was performed, however no external leaks were found. We suspect the gradual pressure increase is either due to our use of in-vacuum optics, optics epoxy adhesive[5], or our use of soldered PCB components.

For optical access, there are two recessed CF100 viewports[6] on the two large faces of the experiment can, see figure A.3. Recessed viewports were required due to the size of the chosen main objectives[7]. These custom objectives have an effective focal length of 33 mm, a working distance of 24.4 mm, and a numerical aperture, NA, of 0.6. They are coated for 397-nm and 729-nm. The consideration for dual high NA objectives is relatively unique in ion trap experiments, and was mainly motivated

---

[4]Scanwel custom housing
[5]EPO-TEK 353ND
[6]UK Atomic Energy Authority P/N VPR100015
[7]Photon Gear custom Atom Imager

by previous work on fast entangling gates via standing waves [13].

There is further optical access via two CF40 side viewports[8] coated for 397-nm, 422-nm, 729-nm, 854-nm and 866-nm, seen in figure A.2. Due to the spatial constraints from the trap assembly and high NA objectives, multiple of our beams must enter the vacuum can through these side ports. For the ion chain to be visible from these side ports, in-vacuum dielectric mirrors are used. These fused-silica mirrors are UHV rated and coated for 372-nm, 397-nm, 422-nm, 729-nm, 854-nm and 866-nm, with reflectivities of >99% for both s- and p-polarised light. Figure A.2 shows a schematic of the beam geometries via the side ports. A limitation of this beam geometry is that due to the permanent B-field direction, it is not possible to provide pure π or $\sigma_\pm$ light to the ion. However for applications where strict polarisation control is needed, the beams can be incident through the CF100 viewport.

An electrical feedthrough on a CF40 flange[9] is used to supply our trap chip and atomic source oven with DC and RF voltages. As the DC cables run within close proximity to the RF supply, electrical pick up is a potential issue for our DC lines. RF leaked onto our DC electrodes will create unwanted pseudopotential which can lead to unexpected mode geometries, or required compensation field. This leakage is mitigated through an in-vacuum RC low pass filter board within close proximity of the trap chip with a cutoff frequency of 17 kHz. The trap chip is mounted onto this filter board via a custom Polyether ether ketone (PEEK) interposer with electric feedthroughs via embedded *Fuzz buttons*[10].

A.4   Imaging System

The imaging system is used to collect fluorescence light from the ion chain for readout, and to image the ion chain for characterisation. We aim for a separation of 5 µm between ions, and require adequate distinguishability of ions in the imaged

---

[8]LewVac ZFSVP-DUV-40CF-OUM
[9]Allectra custom
[10]Custom Interconnects

plane. The system consists of a high quantum-efficiency camera[11], a f=200 mm relay lens, and the f=33 mm NA=0.6 objective. This gives a magnification of 6x, and considering the pixel size of 6.5 µm, leads to a separation of 5 pixels between ions. The objective is on a 5-axis alignment stage with the z-axis focus controlled by a piezo micrometer for fine adjustment of the ion focus.

A.5 Ca^+ Laser Systems

Singly-charged group 2 elements are popular in ion trap experiments due to their single outer electron resulting in Hydrogen-like energy levels. In this thesis we use $^{40}Ca^+$.

$^{40}Ca^+$has no nuclear spin giving the (relatively) simple level structure shown in figure 1.1. The external magnetic field of 5.4 G is applied to split the levels via the Zeeman effect. The relevant laser transitions used in our apparatus are indicated. A zero nuclear spin isotope of calcium was chosen due to this simple level structure without hyperfine splitting. The greater number of levels due to hyperfine splitting lead to more decay paths and therefore greater complications in both cooling and gate schemes. However, due to the lack of hyperfine structure, there are no available magnetic field insensitive transitions, which are often used in ion trap experiments to further decouple the ion from a noisy environment [47].

We define our qubit by the quadrupole transition at 729-nm, which we describe in section 1.1.

Access to other excited levels, outside of our defined two level system, are crucial for ion trap quantum logic to enable qubit readout via state selective fluorescence (397-nm, and 866-nm transitions), and state preparation via optical pumping (397-nm, 866-nm, and 854-nm transitions). Details on these schemes are given in chapter 1. Access to two additional transitions in neutral calcium for isotope selective ionisation, 422-nm and 372-nm, is also required [48].

These transitions (apart from the 729-nm) are all driven by diode lasers[12], which are

---

[11]Hamamatsu Orca-Fusion BT

[12]All Toptica diodes. Red lasers: MDL DL pro; Blue lasers: MDL DL pro HP; 372-nm: iBEAM-SMART-375-S

frequency stabilised to a reference cavity[13] via Pound-Drever-Hall (PDH) locking. PDH locking is used to ensure that laser frequencies are stable to <1 MHz level, well below the natural line widths of all the dipole transitions listed above. The laser frequencies are continuosly monitored with a wavemeter[14].

Frequency and amplitude control for all lasers is achieved via acousto-optic modulators (AOMs) which are driven by Artiq integrated DDS chips, *Urukuls*. The AOMs are used in a double pass configuration to allow shifts of the laser frequency by $\pm \sim 100$ MHz, with no signicant angular shifts or loss of fibre coupling.

A.5.1 Narrow Line Width 729 Laser

Lasers are a key tool for creating the highly localised, strong electric field amplitudes and gradients needed to drive both carrier and sideband transitions of the trapped ion.

As shown in Figure 1.1, two sublevels within the $4S_{1/2}$ to $3D_{5/2}$ manifolds define the qubit. This is an electric quadrupole transition as $\Delta l = 2$. For the Calcium ion this transition is at 729-nm, and so a near resonance 729-nm laser is used to implement single- and multi-qubit gates (sections **??** and 1.4.2). This transition is also used after Doppler cooling for resolved sideband cooling to prepare the motional mode close to its ground state (as discussed in section 1.3.1). This transition is narrrow linewidth due the the long lived $3D_{5/2}$ level, and so, for power efficiency, a narrow linewidth laser must be used. For the "fast entangling gates" use-case, high intensity electric-fields are required at the ion to drive sideband transitions, this will be discussed further in the single-addressing and two-qubit gate sections, but here it is sufficient to say we require >100 mW of light at the ion plane. Here we describe the 729-nm system consisting of a Ti:Sapph laser system pumped with by an Nd:YAG 532-nm laser.

An *M2 Solstis* Ti:Sapph is pumped via 18 W of 532-nm light from a *Coherent Verdi-V* system to produce around 5W of 729-nm light. The Ti:Sapph is engineered to operate with a stable < 50 kHz linewidth. Ti:Sapph crystals have broadband

---

[13]Stable Laser Systems SLS-6010 4-Bore Cylindrical Cavity
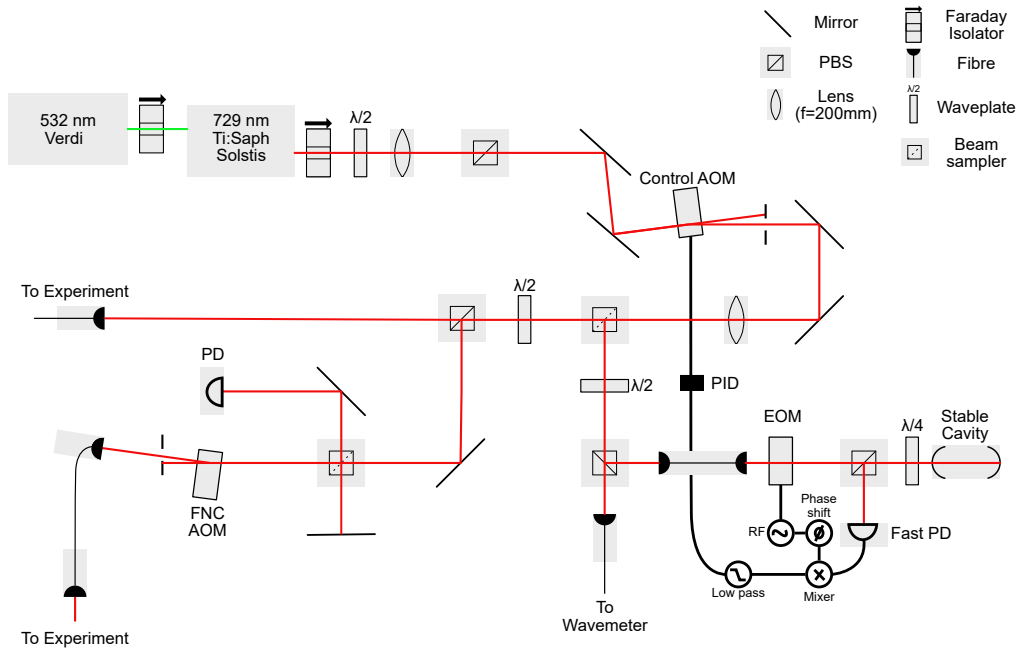[14]HighFinesse WS7

Figure A.4: The 729-nm system. A Ti:Sapph laser tuned to 729-nm is pumped by a 532-nm source. Light is picked off at the first beam sampler to stabilise by PDH locking to a cavity.

gain profiles, which are often exploited in research environments to create frequency tunable laser systems. We however want a narrow linewidth, single frequency laser. The *Solstis* has multiple intracavity frequency selective elements which consist of (in order of coarse frequency selectivity), a birefringent filter, a tunable Fabry-Pérot etalon, and the surrounding bow-tie cavity. For stable single mode operation, the *Solstis* employs an active "dither" servo to lock the peak of etalon transmission to one of the cavity longitudinal mode. This dither consists of periodically varying the etalon spacing with a frequency of around 20 kHz. We must be aware of this dither frequency as the phase modulation leads to the creation of sidebands on our light which can interact with the ion causing unexpected errors in gates. This dither frequency (and harmonics of it), can be observed via composite pulse experiments on the ion, however it is currently not expected to be a limiting source of error in any of the interactions we study.

As mentioned, the *Solstis* alone can operate with linewidths of < 50 kHz, however this linewidth is pushed down further by referencing the Ti:Sapph output to an
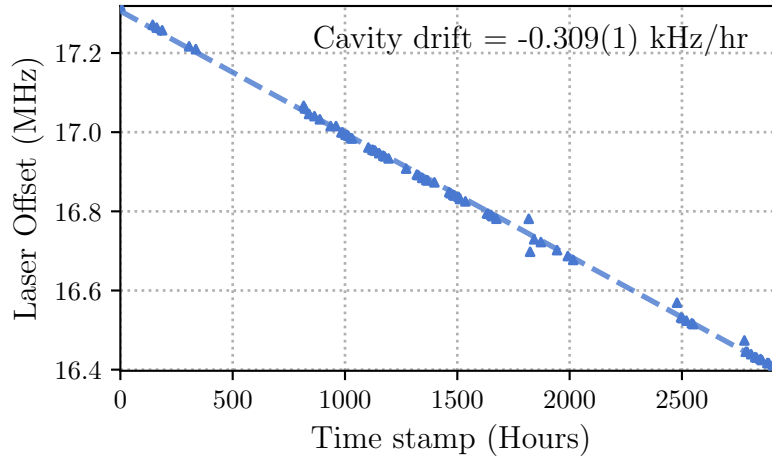
Figure A.5: Cavity drift over 125 days measured by reference to the ion transition. The laser offset here is with respect to running all 729-nm AOMs at their central frequencies. Outliers are due to bad fits of the ion transition frequency, not due to changes in the cavity resonance.

ulta high finesse cavity by *Stable Laser Systems* and applying a Pound-Drever-Hall (PDH) lock [49]. A schematic of the 729-nm system is shown in Figure A.4. PDH locking requires applying two sidebands via an electro-optical modulator (EOM) to the light and directing it onto the stable cavity. The light reflected from the cavity is then directed onto a fast photodetector[15]. The reflection from the cavity consists of the interference between the carrier and the sidebands which have been respectively altered by the cavity transfer function. The photodetector signal is mixed down with the same oscillator signal as provided to the EOM but delayed by some chosen phase, and finally low pass filtered to produce a signal for use as the error signal in the servo loop. This error gives a measure for how far the carrier frequency is from the stable cavity resonant frequency and is used for feedback onto the control AOM situated after the Solstis. With this system, a linewidth of $<< 1$ kHz for the 729-nm light is expected. The electronics for this control loop are provided also by *Stable Laser Systems* in the form of their *FPGA Servo* lock box. For an effective PDH lock, both short and long term stability of the reference cavity is required. To ensure the cavity is insensitive to the environment, it is made

---

[15]Thorlabs PDA10A2

of an ultra low expansion material. The cavity is temperature stabilised at the zero crossing temperature of 30.6°C, and is further isolated by being housed in a vacuum system at $< 1e - 7$ mbar. Long term cavity drifts of 309(1) Hz/hr are measured over 125 days, seen in figure A.5. This measurement uses the ion as a frequency reference to probe the cavity frequency and is discussed in section **??**.

Figure A.4 displays the other beam paths for our 729-nm system. Some light is picked off and sent to a wavemeter to continuosly monitor the frequency. However, the majority is coupled to two output fibres for our experiment and another within the group. The 729-nm light is transported from a dedicated laser lab to a the trap apparatus lab by a 10 m single mode polarization maintaining fibre. The fibre is beneficial in cleaning up the mode from the Ti:Sapph, however it can introduce phase noise due to mechanical and thermal effects along the 10 m length. To remove this introduced noise, passive stabilisation in the form of thick foam tubing along the fibre length, as well as active stabilisation by a fibre-noise-cancellation (FNC) technique [50], is used. We use the *Sinara Stabilizer* [**<empty citation>**] board, a dual channel PID microcontroller, with the *Pounder* [**<empty citation>**] mezzanine board, a dual channel PDH lock generator. The FNC PID software was developed by A. Agrawal. A comparison of spin coherence times is shown in section 1.2.4 with and without fibre noise cancellation enabled.

A.5.2   Single Addressing System

A unique feature of our system is the ability to produce single ion addressing standing waves. The design of this system is shown in figure A.3. A single ion addressing system must be able to illuminate selected ions in the crystal whilst the others remain unperturbed. The advantage of single addressing, other than ion selectivity, is the increased intensity of light due to the tight waist at the ion location.

Our ions are separated by a distance $d \approx 5$ μm. The diffraction limited radius for a collimated 729-nm beam with an objective lens of NA = 0.6 is $\omega_0 = 386$ nm.

Abberations present in real optical components will cause the addressed spot to be increasingly non-Gaussian and lead to unfavourable cross talk at the neighbouring ions. Therefore care was taken in the optical design. See I. Øvergaard Master thesis [15] for relevant design considerations and rationale.

To produce more than one addressed spot and to steer the spots along the ion crystal, Acousto-Optical-Deflectors[16] (AODs) [51, 52] are used. The beam deflection angle is proportional to the drive frequency supplied to the AOD.

---

[16]ISOMET OAD1343-XY-T70S

References

[1] A. M. Steane. "Overhead and noise threshold of fault-tolerant quantum error correction". In: *Phys. Rev. A* 68.4 (2003).

[2] D. J. Wineland et al. "Experimental Issues in Coherent Quantum-State Manipulation of Trapped Atomic Ions". In: *J. Res. Natl. Inst. Stand. Technol.* 103.3 (1998).

[3] A. M. Steane et al. "Speed of ion-trap quantum-information processors". In: *Phys. Rev. A* 62.4 (2000).

[4] V. M. Schäfer et al. "Fast quantum logic gates with trapped-ion qubits". In: *Nature* 555.7694 (2018).

[5] J. I. Cirac and P. Zoller. "Quantum Computations with Cold Trapped Ions". In: *Phys. Rev. Lett.* 74.20 (1995).

[6] A. Sørensen and K. Mølmer. "Entanglement and quantum computation with ions in thermal motion". In: *Phys. Rev. A* 62 (2000).

[7] Y. Liu et al. "Hybrid oscillator-qubit quantum processors: Instruction set architectures, abstract machine models, and applications". In: *arXiv preprint arXiv:2407.10381* (2024).

[8] W. Chen et al. "Quantum computation and simulation with vibrational modes of trapped ions". In: *Chinese Phys. B* 30.6 (2021).

[9] S. Lloyd and S. L. Braunstein. "Quantum computation over continuous variables". In: *Phys. Rev. Lett.* 82.8 (1999).

[10] O. Băzăvan et al. "Squeezing, trisqueezing, and quadsqueezing in a spin-oscillator system". In: *arXiv:2403.05471* (2024).

[11] S. Varona et al. "Towards quantum computing Feynman diagrams in hybrid qubit-oscillator devices". In: *arXiv:2411.05092* (2024).

[12] L. Brenner et al. "Factoring an integer with three oscillators and a qubit". In: *arXiv:2412.13164* (2024).

[13] S. Saner et al. "Breaking the Entangling Gate Speed Limit for Trapped-Ion Qubits Using a Phase-Stable Standing Wave". In: *Phys. Rev. Lett.* 131 (2023).

[14] R. T. Sutherland and R. Srinivas. "Universal hybrid quantum computing in trapped ions". In: *Phys. Rev. A* 104.3 (2021).

[15] I. R. Øvergaard. "Limiting errors of fast entangling gates in trapped ion quantum computers". Master's thesis, Oxford University, UK, 2024.

[16] S. L. Braunstein and R. I. McLachlan. "Generalized squeezing". In: *Phys. Rev. A* 35 (1987).

[17]   A. I. Lvovsky. "Squeezed Light". In: *Photonics*. John Wiley & Sons, Ltd, 2015. Chap. 5.

[18]   C. Flühmann and J. P. Home. "Direct Characteristic-Function Tomography of Quantum States of the Trapped-Ion Motional Oscillator". In: *Phys. Rev. Lett.* 125 (2020).

[19]   P. A. Barton et al. "Measurement of the lifetime of the $3d^2 D_{5/2}$ state in $^{40}Ca^+$". In: *Phys. Rev. A* (2000).

[20]   A. S. Sotirova et al. "High-fidelity heralded quantum state preparation and measurement". In: *arXiv:2409.05805* (2024).

[21]   E. Knill et al. "Randomized benchmarking of quantum gates". In: *Phys. Rev. A* 77 (2008).

[22]   A. C. Hughes. "Benchmarking memory and logic gates for trapped-ion quantum computing". PhD thesis. University of Oxford, 2021.

[23]   D. F. V. James. "Quantum dynamics of cold trapped ions with application to quantum computation". In: *Applied Physics B: Lasers and Optics* 66.2 (1998).

[24]   R. Ozeri. "Tutorial: The trapped-ion qubit toolbox". In: *Contemporary Physics* 52.6 (2011).

[25]   D. J. Wineland and W. M. Itano. "Laser cooling of atoms". In: *Phys. Rev. A* 20.4 (1979).

[26]   M. Ramm et al. "Precision Measurement Method for Branching Fractions of Excited $P_{1/2}$ States Applied to $^{40}Ca^+$". In: *Phys. Rev. Lett.* 111.2 (2013).

[27]   D. C. Morton. "Atomic Data for Resonance Absorption Lines. III. Wavelengths Longward of the Lyman Limit for the Elements Hydrogen to Gallium". In: *ApJS* 149.1 (2003).

[28]   D. M. Meekhof et al. "Generation of Nonclassical Motional States of a Trapped Atom". In: *Phys. Rev. Lett.* 76 (1996).

[29]   A. R. Milne. "Construction of a linear ion trap and engineering controlled spin-motional interactions". PhD thesis. The University of Sydney, 2021.

[30]   Q. A. Turchette et al. "Decoherence and decay of motional quantum states of a trapped atom coupled to engineered reservoirs". In: *Phys. Rev. A* 62.5 (2000).

[31]   P. J. J. O'Malley et al. "Qubit Metrology of Ultralow Phase Noise Using Randomized Benchmarking". In: *Phys. Rev. Appl.* 3.4 (2015).

[32]   P. C. Haljan et al. "Spin-Dependent Forces on Trapped Ions for Phase-Stable Quantum Gates and Entangled States of Spin and Motion". In: *Phys. Rev. Lett.* 94.15 (2005).

[33]   S. C. Burd. "Squeezing and amplification of trapped-ion motion". PhD thesis. University of Colorado at Boulder, 2020.

[34]   C. A. Sackett et al. "Experimental entanglement of four particles". In: *Nature* 404.6775 (2000).

[35]   O. Băzăvan et al. "Synthetic $\mathbb{Z}_2$ gauge theories based on parametric excitations of trapped ions". In: *Commun. Phys.* 7.1 (2024).

[36] C. J. Ballance. *High-Fidelity Quantum Logic in Ca$^+$*. Springer Theses. Springer International Publishing, 2017.

[37] K. Choonee, G. Wilpers, and A. G. Sinclair. "Silicon microfabricated linear segmented ion traps for quantum technologies". In: *2017 19th International Conference on Solid-State Sensors, Actuators and Microsystems*. 2017.

[38] W. Paul. "Electromagnetic traps for charged and neutral particles". In: *Rev. Mod. Phys.* 62.3 (1990).

[39] D. Allcock. "Surface-electrode ion traps for scalable quantum computing". PhD thesis. Oxford University, UK, 2011.

[40] D. Kielpinski, C Monroe, and D J Wineland. "Architecture for a large-scale ion-trap quantum computer". In: *Nature* 417.6890 (2002).

[41] Q. A. Turchette et al. "Heating of trapped ions from the quantum ground state". In: *Phys. Rev. A* 61.6 (2000).

[42] P. See et al. "Fabrication of a Monolithic Array of Three Dimensional Si-based Ion Traps". In: *Journal of Microelectromechanical Systems* 22.5 (2013).

[43] G. Wilpers et al. "A monolithic array of three-dimensional ion traps fabricated with conventional semiconductor technology". In: *Nature Nanotech* 7.9 (2012).

[44] G. Kasprowicz et al. "ARTIQ and Sinara: Open Software and Hardware Stacks for Quantum Physics". In: *OSA Quantum 2.0 Conference (2020), paper QTu8B.14*. 2020.

[45] K. M. Birnbaum. "Ultra-High Vacuum Chambers". In: *unpublished* (2005).

[46] J. Wolf. "Cryogenic, near-field quantum logic chips with passive field nulling on ^{43}Ca$^+$". PhD thesis. University of Oxford, 2019.

[47] S. M. Brewer et al. "^{27}Al$^+$ Quantum-Logic Clock with a Systematic Uncertainty below 10^{-18}". In: *Phys. Rev. Lett.* 123.3 (2019).

[48] D. M. Lucas et al. "Isotope-selective photoionization for calcium ion trapping". In: *Phys. Rev. A* 69.1 (2004).

[49] R. W. P. Drever et al. "Laser phase and frequency stabilization using an optical resonator". In: *Appl. Phys. B* 31.2 (1983).

[50] L. Ma et al. "Delivering the same optical frequency at two places: accurate cancellation of phase noise introduced by an optical fiber or other time-varying path". In: *Opt. Lett.* 19.21 (1994).

[51] W. Nagourney. *Quantum Electronics for Atomic Physics and Telecommunication*. Ed. by Warren Nagourney. Oxford University Press, 2014.

[52] R. Li et al. "A low-crosstalk double-side addressing system using acousto-optic deflectors for atomic ion qubits". In: *arXiv:2306.01307* (2023).